EES Solar

PAPER

View Article Online
View Journal | View Issue

Open Access Article. Published on 01 October 2025. Downloaded on 1/19/2026 7:04:07 PM.
This article is licensed under a Creative Commons Attribution 3.0 Unported Licence.

Check for updates

Cite this: *EES Sol.*, 2025, **1**, 1074

Comparative analysis of recycling strategies for high-yield fabrication of perovskite solar cells: resolving residual impurity challenges *via* targeted post-treatment

Dinesh Kumar,[a] Yeshwanth Nayak Guguloth,[b] Jatindra Kumar Rath *[b] and Trilok Singh *[a]

Received 11th August 2025
Accepted 1st October 2025

DOI: 10.1039/d5el00131e

rsc.li/EESSolar

The sustainable deployment of perovskite solar cells (PSCs) is critically hindered by the lack of efficient recycling strategies for end-of-life (EOL) modules, which pose significant environmental and resource challenges. This work systematically compares conventional single-solvent (SS) recycling with an advanced layer-by-layer multi-solvent (MS) approach to recover functional device components from degraded PSCs. Comprehensive surface and compositional analyses reveal that both SS and MS protocols leave persistent residues, particularly carbon (C), cesium (Cs), and lead (Pb), on the recycled substrates, undermining substrate integrity and limiting their reuse in high-performance devices. To overcome these limitations, we introduce a targeted post-treatment process that eliminates residual contaminants, restoring the substrates to a state comparable to pristine materials. Devices fabricated on these post-treated substrates exhibit a markedly improved fabrication yield and a significantly narrower distribution of power conversion efficiency (PCE) with a variation of just 2.5% across 16 devices, compared to 6% for conventional recycling methods. Furthermore, our techno-economic analysis demonstrates that the proposed recycling protocol reduces the levelized cost of energy by 0.4 to 0.9 ¢ per kWh and shortens the energy payback time by 20 to 40 days relative to modules fabricated on fresh substrates, with module PCE, degradation rate, and system lifetime as key determinants. These findings establish a robust framework for high-yield, economically viable, and environmentally responsible recycling of PSCs, thereby advancing their prospects as a sustainable photovoltaic technology.

Broader context

Photovoltaic modules, designed for 25–30 years of use, often degrade prematurely due to physical, chemical, and environmental stressors. Common issues include potential-induced degradation (PID), light-induced degradation (LID), UV-induced degradation (UVID), and reverse bias degradation, each contributing to significant power losses. Micro-cracks in field-tested modules exacerbate energy loss through increased resistance and hot spot formation. Additional degradation pathways, such as EVA discoloration, encapsulant delamination, busbar corrosion, silver migration, and solder bond failure, often push modules beyond the acceptable annual degradation rate of 0.5–0.7% within the first 5–7 years. Moreover, the perovskite module further suffers from intrinsic material degradation mechanisms. As global deployment accelerates, the volume of PV module waste will surge from 8.0 million tonnes by 2030 to 78 million tonnes by 2050. To address this challenge, jurisdictions are introducing recycling mandates and recovery targets. For instance, the European Union's WEEE directive requires member states to recover 85% of PV module mass and recycle 80%. Recovered materials could be worth over USD 15 billion by 2050, enabling the production of approximately two billion new modules or redistribution to other markets. Therefore, establishing robust recycling protocols offers significant promise and demands prompt focus from the research community.

Introduction

End-of-life solar modules pose a significant environmental challenge in the emergent photovoltaic (PV) technologies, as their disposal in landfills introduces resource depletion, toxicity, and other potential environmental hazards. Implementing the circular economy principle by recovering crucial raw materials used in their construction can significantly reduce the levelized cost of electricity and energy payback time[1,2] across various solar cell technologies, thus establishing sustainable practices and the potential of reducing human toxicity impacts by 68.8%.[3–5] Perovskite solar cells have emerged as a promising PV technology, offering a high-power conversion

[a]*Semiconductor Thin Film and Emerging Photovoltaic Laboratory, Department of Energy Science and Engineering, Indian Institute of Technology Delhi, New Delhi-110016, India. E-mail: trilok.singh@dese.iitd.ac.in*

[b]*Department of Physics, DSEHC, Indian Institute of Technology Madras, Tamil Nadu-600 036, India. E-mail: jkr@faculty.iitm.ac.in*

© 2025 The Author(s). Published by the Royal Society of Chemistry

Open Access Article. Published on 01 October 2025. Downloaded on 1/19/2026 7:04:07 PM.
This article is licensed under a Creative Commons Attribution 3.0 Unported Licence.

efficiency of >26%.[6] However, the widespread adoption of PSCs faces two significant challenges, the high cost and scarcity of materials associated with the use of float glass, fluorine tin oxide (FTO), indium-doped tin oxide (ITO) as a transparent conducting oxide (TCO), metal contacts, and the environmental concerns surrounding the presence of toxic Pb in the perovskite absorber layer.[7–10] Before widespread commercialization, addressing these issues is crucial for the sustainable and economically viable large-scale deployment of perovskite module technology. Numerous studies have highlighted the raw material cost distribution of individual components in a prototype n-i-p structured PSCs, where the TCO, hole transport layer (HTL), such as spiro-OMeTAD, and metal electrodes like gold (Au) or silver (Ag) constitute significant portions of the total raw material cost. Wang *et al.*[11] concluded that these components make up 30%, 53%, and 16% of the total raw material cost, respectively. Augustine *et al.* estimated FTO, having a sheet resistance of approximately 14 $\Omega\ \square^{-1}$, costs around \$285 per m^2.[12] Huang *et al.*[13] highlighted that ITO accounts for approximately 51.2% of the overall material cost. Larini *et al.*[14] predicted that TCO-coated glasses constitute 56% of the total cost of a perovskite module and 96% of its carbon footprint. Binek *et al.*[9] also calculated that the hole-transporting material spiro-OMeTAD and Au electrode are the major cost factors, with potential replacements being considered for future scalability. Thus, recovering the TCO-coated glass from the EOL device is important for the sustainable development of PSCs. Most studies on various other PV module recycling methods involve the mechanical crushing of the cells and subsequent high-temperature/energy-intensive processing.[15,16] Various solar technologies, such as CdTe,[17–21] CIGS,[22–28] silicon, and tandem solar cells at the lab scale, have also established high-yield recycling processes.[29–31] However, among emerging technologies such as PSCs, recycling the EOL device is more feasible due to the capability of solution processing of overall PSCs. Several researchers have reported recycling EOL devices by reverse engineering the fabrication protocols of PSCs.[9,12,32,33] This involves dissolving the widely used HTL spiro-OMeTAD in chlorobenzene (CB), the perovskite layer in dimethylformamide (DMF) or dimethyl sulfoxide (DMSO), and the electron transport layer (ETL) in subsequent solvents with extended ultrasonication times.[9,12] Consequently, the recovered FTO or FTO/ETL (for regular structured devices) and FTO/HTL (for inverted structured devices) can be reutilized to construct fresh devices. Furthermore, researchers have explored and upscaled the extraction of raw materials such as HTL,[11] perovskite precursor (PbI_2),[34] and expensive TCO substrates in refabricating PSCs. The research efforts in recycling PSCs can be broadly classified into two distinct categories. The first is single-solvent (SS) recycling, which dissolves the full device in a single solvent. Dissolution of the different layers in selective solvents such as spiro-OMeTAD, MAI, FAI, CsI, and PbI_2 in different solvents can be termed multi-solvent (MS) recycling of the perovskite device. In SS recycling, various solvents such as KOH,[12] methylamine,[11] DMF,[9,13,35] DMSO,[14] butylamine,[32,36] choline chloride, ethylene glycol (EG),[37] aqua regia,[38] γ-butyrolactone,[39] and numerous others have been investigated, yielding positive outcomes in recycling the expensive substrate as well as other components of PSCs. In the MS or selective dissolution recycling process, adhesive tape for Au removal, solvents such as ethyl acetate for Au removal and delamination, dichlorobenzene (DCB)[34] and CB[3,40] for HTL dissolution, DI water[40] and ethanol[3] for dissolution of organic components of perovskite, and DMF and DMSO[3,14,34,39–42] for PbI_2 dissolution are explored by researchers. DMSO has also been reported to have the lowest total environmental impact and being least harmful to human health among the DMSO, DMF, *N*,*N*-dimethylacetamide (DMAC), *N*-methyl-2-pyrrolidone (NMP), 1,3-dimethyl-3,4,5,6-tetrahydropyrimidin-2(1*H*)-one (DMPU), gamma-butyrolactone (GBL), tetrahydrofuran (THF), 1,3-dimethylimidazolidin-2-one (DMI) solvents.[43] Prior studies have highlighted the reuse of FTO/ETL[44,45] substrates *via* single- and multi-solvent recycling and compared these approaches; in contrast, the present work specifically focuses on the end-of-life perovskite residues that remains on the substrate. Numerous studies have also highlighted the presence of sticky residual perovskite precursor impurities C, Cs, Pb, and I on the substrate despite post-processing the recovered substrate with acetone, isopropyl alcohol (IPA), and DI water. These studies also reported that even after ultrasonication and post-cleaning of the substrate, the residues stick to the substrates, as revealed by X-ray photoelectron spectroscopy (XPS) measurements.[11,12,14,35,36,39,46] However, a direct comparison between SS and MS recycling and their impact on the recycled FTO/ETL substrate has not been explored in the literature until now. While the MS recycling procedure can be more beneficial for implementing the circular economy principle, the simultaneous comparison of SS recycling with MS recycling and the removal of residual impurities for the reliable fabrication of the PSC is the essence of this study. During this investigation, we examined the impact of transitioning from SS to MS recycling on the FTO/ETL substrate and uncovered several novel findings. Quantitative XPS analysis revealed that SS recycling leaves residual Pb, C, and Cs concentrations on FTO/ETL substrates. In contrast, in MS recycling, the presence of Pb on the substrate was significantly diminished, further reduced by introducing a novel step in the recycling process, *i.e.*, post-treatment of the MS processed substrate with the widely available laboratory chemicals, diluted potassium hydroxide (KOH) and hydrochloric acid (HCl) sequentially. The detected Pb content in the post-processed case (target sample) was notably at an ultra-low level, and other residual impurities were removed entirely from the substrate. Our study's central goal is to remove these residues through post-processing using a combination of KOH and HCl, enabling recovery of the substrates under as close to pristine conditions as possible for reuse in new devices. Perovskite film growth on recycled substrate was observed to be polycrystalline with minimum impurity phases. Our findings also highlighted the issues concerning the reproducibility of obtaining high device efficiency when utilizing SS recycled substrates, in contrast to the target sample. The additional step introduced during MS recycling drastically reduced Pb content, resulting in highly efficient and reproducible devices. This observation is particularly desirable for establishing a high process yield in the recycling process,

Open Access Article. Published on 01 October 2025. Downloaded on 1/19/2026 7:04:07 PM.
This article is licensed under a Creative Commons Attribution 3.0 Unported Licence.

which is highly desirable for commercializing PSC and implementing recycling solutions for large-scale applications, as the EU's WEEE directive requires 85% recovery of the waste generated due to PV modules.[47] Lastly, our techno-economic analysis predicted the benefits of recycling various components of PSCs for utility-scale installation and predicted a cost curve to yield the maximum benefit of the recycling process.

Results and discussion

Recycling process

Fresh PSCs were fabricated using the process described in the Experimental section with the device structure FTO/SnO_2/perovskite/spiro-OMeTAD/Au electrode. Various samples deposited on the fresh substrate FTO/SnO_2 are termed 'fresh' throughout the manuscript. After a 50% efficiency loss, the EOL unencapsulated devices were used to recycle the FTO/SnO_2 substrate for subsequent deposition of the complete cell. As previously proposed, in the SS recovery of the substrates, the Au electrode was first peeled off using Scotch tape. DMSO solvent was selected based on the criteria of green, and high-polarity aprotic solvent, to dissolve the perovskite lattice.[43,48,49] Lastly, SS-processed substrates were cleaned using DI water, acetone, IPA, and ultraviolet ozone (UVO) treatment before refabricating the fresh devices on recycled substrates. These samples are termed 'SS' in the manuscript. For the MS recycling procedure, the Au electrode was first peeled off using Scotch tape and subsequently delaminated in ethyl acetate. After this step, for HTL (spiro-OMeTAD) dissolution, devices were kept in chlorobenzene (CB) and sonicated for 10 minutes. For MAI, FAI, and CsI dissolution, devices were submerged in DI water and sonicated for 10 minutes. After that, PbI_2 was removed using the DMSO solvent. These samples are termed 'MS' in the manuscript. Fig. S1 in the SI shows a sequential recovery workflow starting with collected EOL PSC cells, followed by key steps of the recycling process. After MS processes, the target substrates were briefly submerged in diluted KOH and HCl; these samples are termed 'target' in the manuscript. The detailed experimental protocol is listed in the Experimental section. Fig. S2 shows that the MS recycling process discussed above is highly selective for removing the layer-by-layer extraction, and the cross-sectional scanning electron microscope (SEM) imaging confirmed this trend. Fig. S2a shows the cross-sectional image of the PSC just before the EOL. Fig. S2b shows the device's cross-sectional image after removing the Au electrode using Scotch tape and ethyl acetate delamination, and the device is stacked up to the HTL only. After Au removal and delamination, the HTL was dissolved in CB, and Fig. S2c shows the remaining perovskite-coated substrate. Lastly, the perovskite layer was dissolved in DI water, and DMSO subsequently caused the dissolution of the remaining perovskite on FTO/ETL substrate, as shown in Fig. S2d. Fig. 1 presents a flowchart detailing the recycling process for various photovoltaic technologies, including CdTe, CIGS, PSC, and silicon-based cells, each with its distinct recycling pathway. PSC recycling stands out for its efficiency and environmental friendliness. Its key advantage lies in selective solvent dissolution, enabling layer-by-layer separation of components while preserving substrate integrity. This

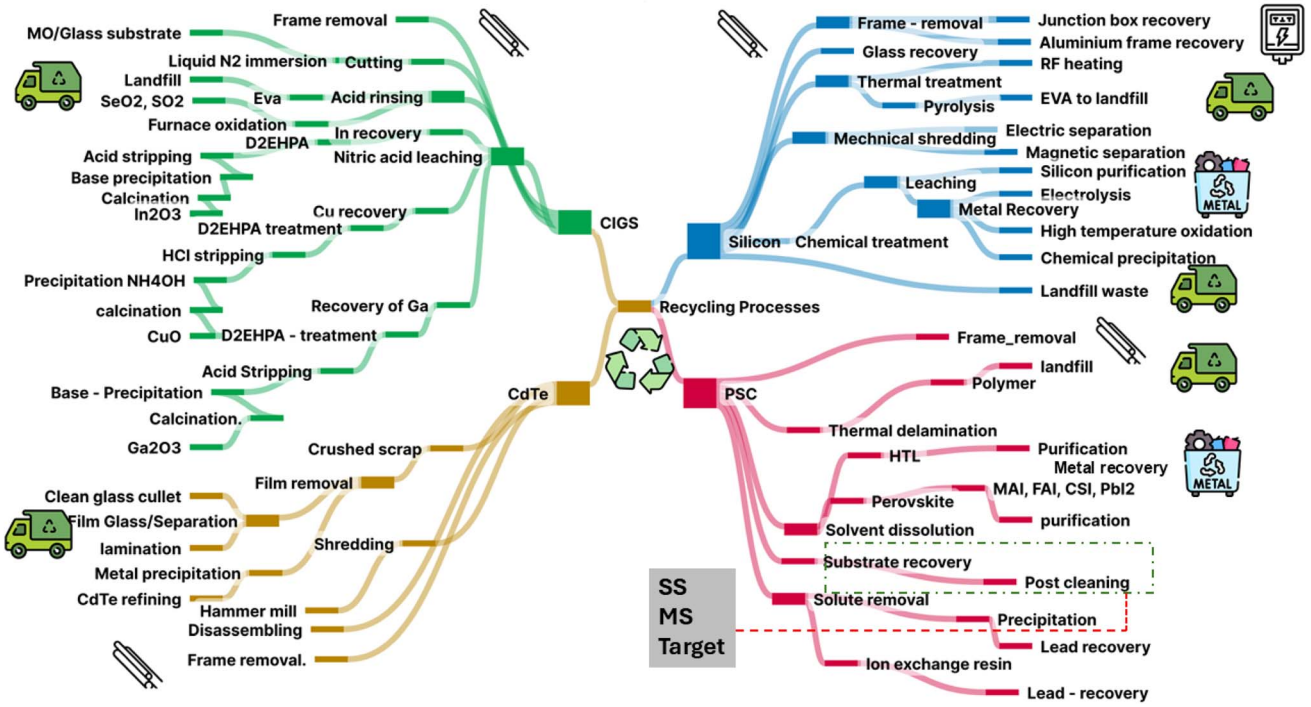

Fig. 1 Overview of recycling processes for various PV technologies, including silicon-based solar cells, PSCs, copper indium gallium selenide (CIGS), and cadmium telluride (CdTe) solar cells. The diagram categorizes recycling steps into key stages. The various recycling steps for different technologies were collected using ref. 51–59.

 © 2025 The Author(s). Published by the Royal Society of Chemistry

Open Access Article. Published on 01 October 2025. Downloaded on 1/19/2026 7:04:07 PM.
This article is licensed under a Creative Commons Attribution 3.0 Unported Licence.

non-destructive method allows precise targeting of functional layers and maintains material value. The approach facilitates the separate recovery of the perovskite layer, transport layers, and the substrate without damage. The PSC branch in the figure shows a more straightforward, solvent-based process mainly occurring at room temperature or with minimal heating, avoiding energy-intensive crushing or shredding. This method achieves nearly complete material recovery up to 99.2% efficiency for Pb components.[50] In contrast, other PV technologies use more destructive, energy-intensive methods. Silicon cells require harsh chemical treatments and high-temperature processes, while CdTe cells involve aggressive sulfuric acid and hydrogen peroxide treatments, along with multiple thermal and leaching steps. The environmental impact of HCl and the reclaimed TCO-coated glass substrate is presented in the SI.

Impact of recycling processes on substrates

To explore the efficacy of the recycling process in removing residual impurities *via* various recycling processes, we first measured the contact angles of the various samples. The contact angle is a critical parameter that indicates the wettability of a surface, which affects the adhesion and spreading of liquids on solid substrates[60] and can also be used to gauge the presence of residual perovskite impurities on various substrates. Fig. 2a illustrates the comprehensive model for the proposed target recycling strategy of perovskite solar cells. The schematic outlines the materials, solvents, and sequential steps involved in the recycling and post-treatment to recover high-quality substrates for device refabrication. The innovative step in the proposed model is a targeted post-treatment using diluted KOH and HCl, which effectively removes persistent contaminants. We hypothesize that KOH and HCl play complementary roles in targeted residue removal. KOH is a strong alkaline agent that effectively breaks down contaminants such as carbon-based compounds. HCl is a strong mineral acid commonly used to dissolve and remove hydroxides and other inorganic metal residues from the surfaces. Fig. 2b shows the contact angle measurement of perovskite precursor ink on a fresh FTO/SnO_2 substrate as a reference sample. The contact angles measured on both sides of the droplet are 13.79° and 13.67°, indicating a hydrophilic surface. Fig. 2c suggests a substrate subjected to an MS recycling process. The contact angles for these samples are 7.97° and 8.67°, which are lower than those of the fresh substrate. The reduced contact angles suggest increased surface hydrophilicity due to the organic and inorganic residues that alter the surface energy. Due to the presence of perovskite residues, the SS-processed substrate using DMSO showed extreme hydrophilicity towards perovskite ink, as shown in Video V1, provided in the SI. Lastly, Fig. 2d shows the target sample that underwent post-treatment with KOH and HCl after the MS recycling process. This post-treatment removes residual elements that have remained on the substrate after the MS process. The contact angles are 11.02° and 10.96°, higher than those of the MS recycled sample, approaching those of the fresh substrate. This indicates that the

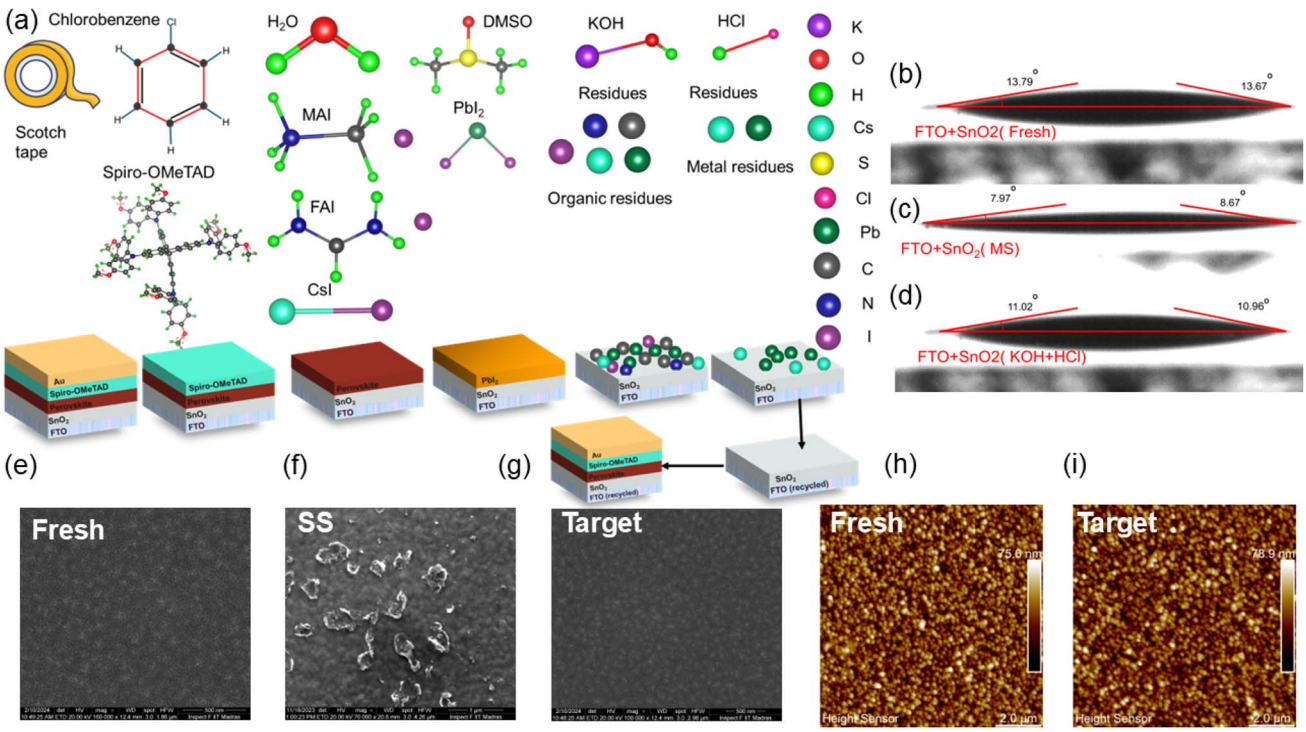

Fig. 2 Comparative analysis of FTO/SnO_2 substrates during the PSC recycling process. (a) Schematic model of the recycling procedure proposed in this work with various materials. (b–d) Contact angle measurements of the triple cation perovskite precursor on the (b) fresh FTO/SnO_2 substrate, (c) MS processed substrate, and (d) target substrate treated with KOH + HCl. (e–g) SEM images of the (e) fresh substrate, (f) SS processed substrate, and (g) target substrate. (h–i) AFM topographic images of the (h) fresh SnO_2 ETL substrate and (i) target substrate.

Open Access Article. Published on 01 October 2025. Downloaded on 1/19/2026 7:04:07 PM.
This article is licensed under a Creative Commons Attribution 3.0 Unported Licence.

post-treatment has effectively cleaned the surface, restoring it to its original hydrophilicity compared to the MS and SS-processed substrates. Fig. 2e–g show the SEM images of these substrates and explore the features of the recycling process. Fig. 2e shows a large, uniform, and featureless area, indicating a smooth or flat fresh FTO/SnO_2 substrate surface, and the substrate appears free of significant defects or contamination, which is desirable for the initial fabrication of the PSCs. Fig. 2f shows a more textured or granular surface with numerous small particles dispersed across the area. It shows the presence of large agglomerated residual impurities on the SS substrate compared to fresh and target substrates. These features suggest a heterogeneous or rough surface attributed to impurities or residues left from the EOL perovskite device after the SS recycling process. Fig. 2g indicates that the target recycling process has removed significant impurities compared to the SS-processed substrate, resulting in a cleaner surface. To qualitatively and quantitatively analyze the presence of various residual impurities on different substrates, we performed the energy dispersive X-ray spectroscopy (EDX), elemental mapping, and XPS measurements of multiple samples. Fig. S3a presents the EDX spectrum of a sample processed through the SS recycling method. The spectrum shows prominent peaks corresponding to tin (Sn) and oxygen (O), and noticeable peaks for Pb, suggesting that Pb from the perovskite material remains on the substrate after the SS recycling process, and shows the elemental composition of the SS-processed substrate determined using EDX. Fig. S3b presents the EDX spectrum of a target substrate. The spectrum again shows peaks for Sn and O, which are consistent with the presence of SnO_2. The Pb peaks appear to be eliminated compared to the SS samples, suggesting that the target treatment effectively reduces Pb contamination on the substrate. Furthermore, Fig. S4a–c show the elemental mapping of Pb on a substrate undergoing SS, MS, and target recycling processes. The mapping is visualized as a distribution of red dots across a dark background, where the intensity of the red color corresponds to the concentration of Pb present on the substrate. The SS map in Fig. S4a indicates the significant presence of Pb, suggesting that the SS process is ineffective in removing Pb from the substrate. Fig. S4b presents the elemental mapping of Pb on a substrate treated with an MS recycling process; the intensity and distribution of the red dots are less pronounced than the SS sample, implying that the MS process is more effective at reducing Pb contamination, although some Pb remains during the process. Fig. S4c shows the elemental mapping of Pb on a substrate that has undergone a targeted treatment. The red dots in this image are sparse and less intense, indicating a substantial reduction/elimination of Pb present on the substrate. Tables S1 and S2 shows the quantitative elemental composition of SS and the target substrate determined through EDX measurement. We measured fresh and target samples using an atomic force microscope (AFM) to estimate the effect of target recycling processes further. Fig. 2h shows the 2D AFM scan of a fresh FTO/SnO_2 substrate. The surface appears relatively smooth with a fine, granular texture.[61] The root mean square (RMS; R_q) surface roughness is 11 nm, typical for ETL thin films used in PSCs. Fig. 2i presents a 2D AFM scan of FTO/SnO_2 for the target substrate, which shows a slightly more pronounced texture than the fresh substrate, with an R_q of 12 nm. The increase in roughness could be due to the etching effect of the chemical treatment, which modifies the surface topography. Fig. S5a and b show 3D AFM representations of the fresh and target substrates, providing a visual perspective of the surface peaks and valleys. Other values of AFM statistical parameters of these substrates are listed in Table S3. Fig. S5c shows the XRD patterns of the fresh and target FTO/SnO_2 substrates. Both substrates exhibit similar patterns of several distinct peaks at specific 2θ angles, which correspond to the planes of the crystal lattice, labeled with their respective Miller indices such as (110), (101), (200), (211), (220), (310), and (301) corresponding to the tetragonal phase of the thin film.[62] The similarity in peak positions between the fresh and recycled samples suggests that the recycling process preserves the crystalline structure of the FTO/SnO_2 substrate. The lattice parameters for target substrates are $a = b = 4.76$ Å; $c = 3.18$ Å. Furthermore, the microstrain of magnitude of $\sim 4 \times 10^{-2}$ for the target substrate and average crystallite size in the range of ~15.5 nm were determined using Williamson–Hall analysis.[63]

XPS survey scans were obtained for a comprehensive overview of the elemental composition and chemical states of FTO/SnO_2 substrates undergoing different recycling processes. Fig. S6a presents a comparative survey scan of the MS, SS, and target samples. Fig. S6b focuses on the SS-processed substrate, confirming the presence of elements such as Sn, O, nitrogen (N), Pb, Au, Cs, and C peaks suggest that the SS recycling leaves significant impurities on the substrate. Fig. S6c shows the XPS spectrum for the MS-processed substrate. Like the SS sample, there are peaks present for Sn, O, Pb, and C. It does not eliminate them, as evidenced by the persistent presence of Pb and C. Fig. S6d shows a survey scan of the target sample with reduced intensity of impurity peaks and does not show signs of N, Au, C, or Cs peaks.

Fig. 3a and b present an XPS analysis of Sn 3d for fresh and target samples, and the peak deconvolution is shown in Fig. S7a and b. Fig. 3a shows the characteristic Sn 3d doublet with two prominent peaks: the Sn $3d_{5/2}$ peak and the Sn $3d_{3/2}$ peak, consistent with the spin–orbit coupling effect observed in 3d orbitals. Fig. S7a presents the deconvolution of the Sn $3d_{5/2}$ peak into its constituent different oxidation states[64] of tin: Sn^{4+}, Sn^{2+}, and metallic Sn^0. The Sn^{4+} species appear at a binding energy of 485.27 eV with a full width at half maximum (FWHM) of 1.26 eV and dominating the spectrum with 73.8% of the total Sn $3d_{5/2}$ area. The metallic tin (Sn^0) component is positioned at 484.97 eV and has a narrower FWHM of 0.85 eV with 0.5% of the total area. The intermediate Sn^{2+} oxidation state appears at 485.31 eV and has a notably broader FWHM of 2.43 eV, suggesting greater chemical or structural heterogeneity for this species with a 25.7% contribution to the total area. The dominance of Sn^{4+} aligns with the expected stoichiometry of pristine SnO_2, while the minor Sn^{2+} and Sn^0 components suggest slight surface reduction. The broader Sn^{2+} peak implies structural disorder or heterogeneous bonding environments.[65,66] Fig. 3b presents XPS data for the target sample. Similar to the fresh

 © 2025 The Author(s). Published by the Royal Society of Chemistry

Open Access Article. Published on 01 October 2025. Downloaded on 1/19/2026 7:04:07 PM.
This article is licensed under a Creative Commons Attribution 3.0 Unported Licence.

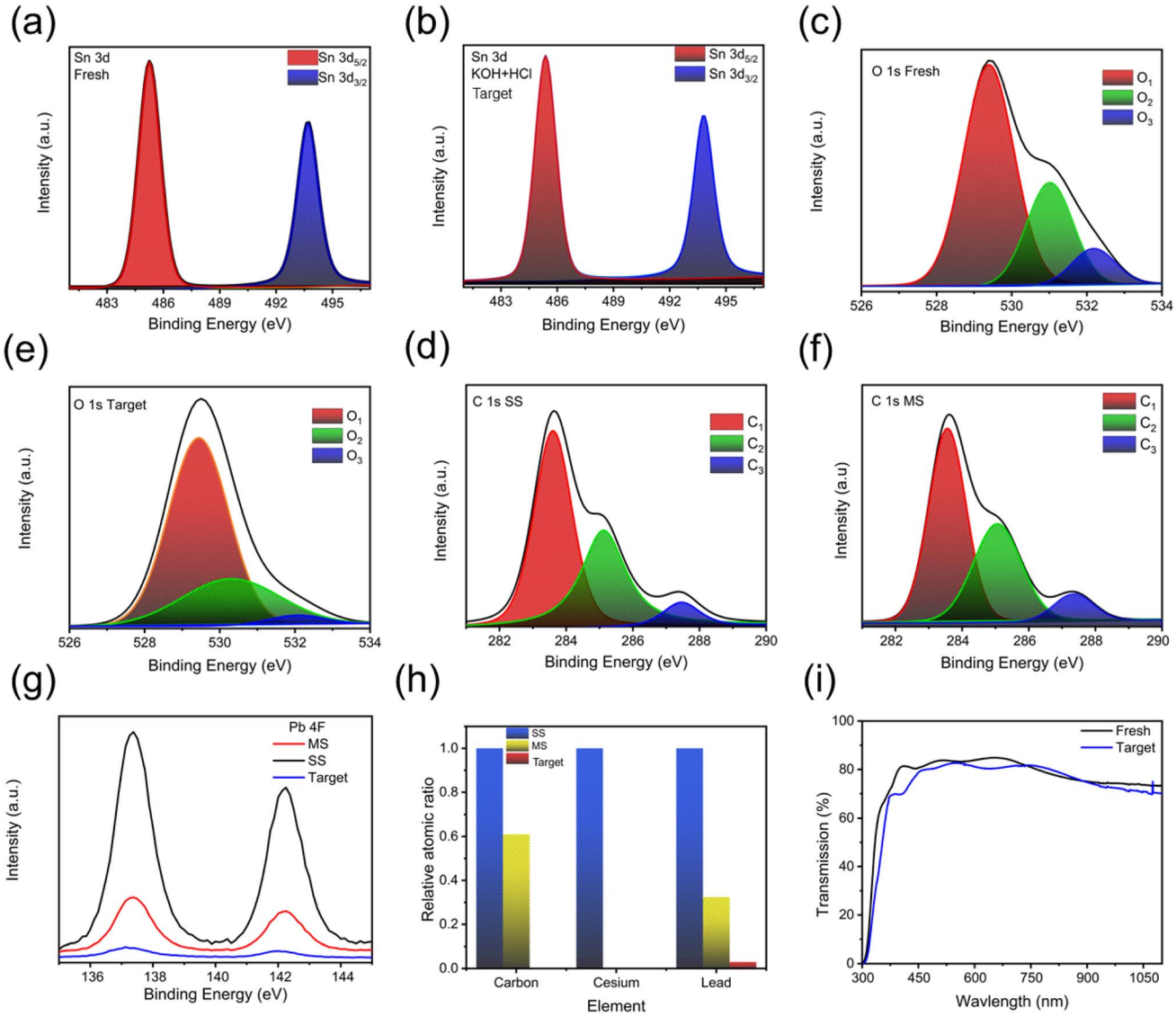

Fig. 3 Comprehensive characterization of fresh and post-treated FTO/SnO_2 substrates using various spectroscopic techniques. (a–d) XPS core-level spectra showing: (a) Sn 3d spectrum of the fresh FTO/SnO_2 substrate with characteristic Sn $3d_{5/2}$ and Sn $3d_{3/2}$ peaks, (b) Sn 3d spectrum of the target post-treated substrate, (c) O 1s spectrum of the fresh substrate, and (d) O 1s spectrum of the target substrate. (e and f) C contamination analysis: (e) C 1s spectrum of the SS processed substrate and (f) C 1s spectrum of the MS processed substrate. (g) Pb 4f core-level spectra of SS, MS, and target samples. (h) Relative atomic concentration ratios of C, Cs, and Pb across SS, MS, and target samples. (i) Optical transmission spectra comparing fresh and target substrates.

sample, the target sample exhibits the characteristic Sn 3d doublet with Sn $3d_{5/2}$ and Sn $3d_{3/2}$ peaks. Fig. S7b shows the deconvolution of the Sn $3d_{5/2}$ peak into its constituent chemical states with the Sn^{4+}, Sn^{2+}, and Sn^0 peaks. The deconvolution of the target substrate reveals notable differences compared to the fresh sample. The Sn^{4+} component appears at 485.26 eV with an FWHM of 1.17 eV, showing a slight shift in binding energy and a reduction in area compared to the fresh sample, with a 64.1% contribution of Sn $3d_{5/2}$. The Sn^{2+} species is positioned at 485.54 eV with an FWHM of 1.46 eV, indicating a significant binding energy shift and an increase in relative proportion compared to the fresh sample, with 33.1% of the total area. The metallic Sn^0 component appears at 484.02 eV with a small area compared to fresh samples, with a 2.8% contribution. The fresh sample shows a predominance of the Sn^{4+} oxidation state (typical for SnO_2), with a smaller contribution from Sn^{2+} and the presence of metallic Sn^0. In contrast, the target sample exhibits a more balanced distribution between Sn^{4+} and Sn^{2+} states, suggesting a partial reduction of the Sn species during treatment. The relative areas of these peaks provide quantitative evidence for this chemical transformation, with the $Sn^{4+}:Sn^{2+}$ ratio decreasing from approximately 2.9 : 1 in the fresh sample to 1.3 : 1 in the target sample. The binding energy positions also show subtle but significant shifts between the samples, particularly for the Sn^{2+} and Sn^0 components, indicating changes in the chemical environment surrounding Sn species after

Open Access Article. Published on 01 October 2025. Downloaded on 1/19/2026 7:04:07 PM.
This article is licensed under a Creative Commons Attribution 3.0 Unported Licence.

treatment. These shifts, coupled with the changes in FWHM values, suggest structural reorganization and changes in the local coordination chemistry of Sn atoms in the treated sample. The narrowing of Sn^{2+} peak and reduction in FWHM from 2.43 eV to 1.47 eV, suggesting a more uniform chemical environment after treatment. The chemical treatment induces a pronounced Sn^{2+} enrichment. The stable Sn^{4+} peak FWHM (~1.2 eV) reflects retaining of SnO_2 domains despite chemical treatments. The narrowing of Sn^{2+} peak FWHM (2.43 eV → 1.47 eV) implies homogenization of Sn^{2+} sites. Fig. 3c and d show the high-resolution XPS spectrum of the O 1s region from a fresh SnO_2 sample, spectral data exhibiting an asymmetric profile that indicates the presence of multiple O species. The deconvolution analysis has resolved this complex peak into three distinct components, each representing a specific O chemical environment in the SnO_2 lattice.[67] The dominant component, O_1, is centered at approximately 529.5 eV; this peak corresponds to lattice oxygen bonding in the SnO_2 crystal structure, representing O^{2-} ions bound to the Sn^{4+} state. The second component, O_2, indicates oxygen vacancies, and O_3 corresponds to hydroxyl groups.[68] The target sample in Fig. 3d exhibits a redistribution of these O components, with O_1 showing a 7.10% increase in area under the curve. In comparison, the area under the curve for O_2 marginally increases by 1.66%, and the area under the curve for O_3 dramatically decreases to 56.45% after baseline correction. This significant depletion of hydroxyl groups (O_3) in the target sample indicates effective dehydroxylation of the surface during target treatment, thus reducing the presence of hydroxyl groups on the surface of SnO_2. Simultaneously, the relative increase in lattice oxygen (O_1) and modest growth in oxygen vacancies (O_2) suggest restructuring of the oxide framework. We speculate that these films bear surface –OH groups that block reactive sites and leave most tin as Sn^{4+}. Upon KOH exposure, K^+ ions coordinate with surface hydroxyls to form KOH *in situ*, weakening Sn–O bonds and loosening the hydroxyl network. This priming step renders the surface more susceptible to oxygen removal. Subsequent HCl treatment provides H^+ ions that neutralize the remaining OH^- groups ($H^+ + OH^- \rightarrow H_2O$) and Cl^- ions that transiently interact with Sn sites. The acid-mediated dehydroxylation strips surface hydroxyls and creates oxygen vacancies (V_O), each of which releases two electrons. To preserve electrical neutrality, neighboring Sn^{4+} ions capture these electrons and reduce to Sn^{2+}. Thus, the KOH step softens the surface bond framework, and HCl completes dehydroxylation and vacancy creation, culminating in a substantial increase in reduced tin species. This combined chemical sequence not only cleanses the surface but also enriches Sn^{2+} and oxygen vacancies, optimizing the electronic properties of recycled SnO_2 for high-performance perovskite solar cell applications. Fig. S7c shows the Cs XPS spectrum for the SS-processed substrate. The broad peak observed in the Cs 3p core level region indicates the presence of Cs on the substrate surface. Cs is used in the perovskite triple cation perovskite absorber layer to improve the device efficiency[69] and stability under air ambient conditions.[70] However, its presence in the recycled substrate indicates residue from the EOL device, suggesting incomplete removal during the SS recycling process. These residual impurities potentially interfere with the formation of the perovskite layer and affect the overall device performance, as seen later in the *J–V* response of the PSCs. Fig. 3e and f display the C 1s signal arising from EOL residual impurities, which can be attributed to adventitious carbon and distinct functional groups (–C–C, –C=NH_2^+, and –C–NH_2) expected from methylammonium/formamidinium degradation. The aim of the combined protocol was to remove both forms of carbon, *i.e.*, originating from perovskite and from adventitious sources, as further verified by Fig. S6 in the SI. Fig. 3g presents the XPS spectra of the Pb 4f region for different samples processed by SS, MS, and a targeted treatment. The spectra exhibit two distinct peaks corresponding to the Pb $4f_{7/2}$ and Pb $4f_{5/2}$ components, characteristic of Pb in samples.[71] The SS sample exhibits the highest Pb 4f peak intensity, indicating the maximum Pb concentration. The MS sample shows lower intensity, suggesting reduced Pb concentration compared to SS. The target sample has the lowest Pb 4f peak intensity, indicating negligible Pb concentration. This demonstrates that the target treatment is the most effective in removing Pb, making the substrate more suitable for fabricating new PSCs. The SS exhibits a notably large area under the curve, suggesting substantial Pb retention from the original perovskite composition. The MS-processed sample shows significantly reduced peak intensities, with the area under the curve of approximately 25% of the Pb content found in the SS sample. The target sample shows minimal peak intensities, with the area under the curve indicating that its Pb content is about 5.4% relative to that of the SS sample. Fig. 3h is a bar graph showing the relative atomic concentration ratios of C, Cs, and Pb detected on the samples during the XPS study. The SS sample has the highest relative atomic concentration of Pb, as indicated by the tallest bar in the graph, while the target sample has the least. Furthermore, no C and Cs signatures were observed in the target samples. Lastly, Fig. 3i shows the optical transmission spectra of fresh and target samples across the visible wavelength range. The similarity of transmission spectra for fresh and recycled FTO substrates prominently indicates that the optical transmission of the FTO is retained after recycling. Both samples exhibit higher transmission across most visible and near-infrared regions, peaking at approximately 85% around 600 nm.

Perovskite deposition on substrates

To compare the performance of recycled substrates for device application, we studied the fresh *vs.* target substrates for perovskite layer deposition using various characterization tools. Fig. 4a shows the nearly identical absorbance curves for fresh and target samples, indicating excellent reproducibility between the fresh and target samples using the recycling methodology. The strong absorption across the visible spectrum indicates excellent light-harvesting capabilities in this range for both samples. Fig. 4b shows the XRD pattern for fresh and target samples, indicating a pseudo-cubic crystal structure,[72] typical for triple cation perovskite compositions. Both samples showed the presence of well-defined peaks indexed to

 © 2025 The Author(s). Published by the Royal Society of Chemistry

Open Access Article. Published on 01 October 2025. Downloaded on 1/19/2026 7:04:07 PM.
This article is licensed under a Creative Commons Attribution 3.0 Unported Licence.

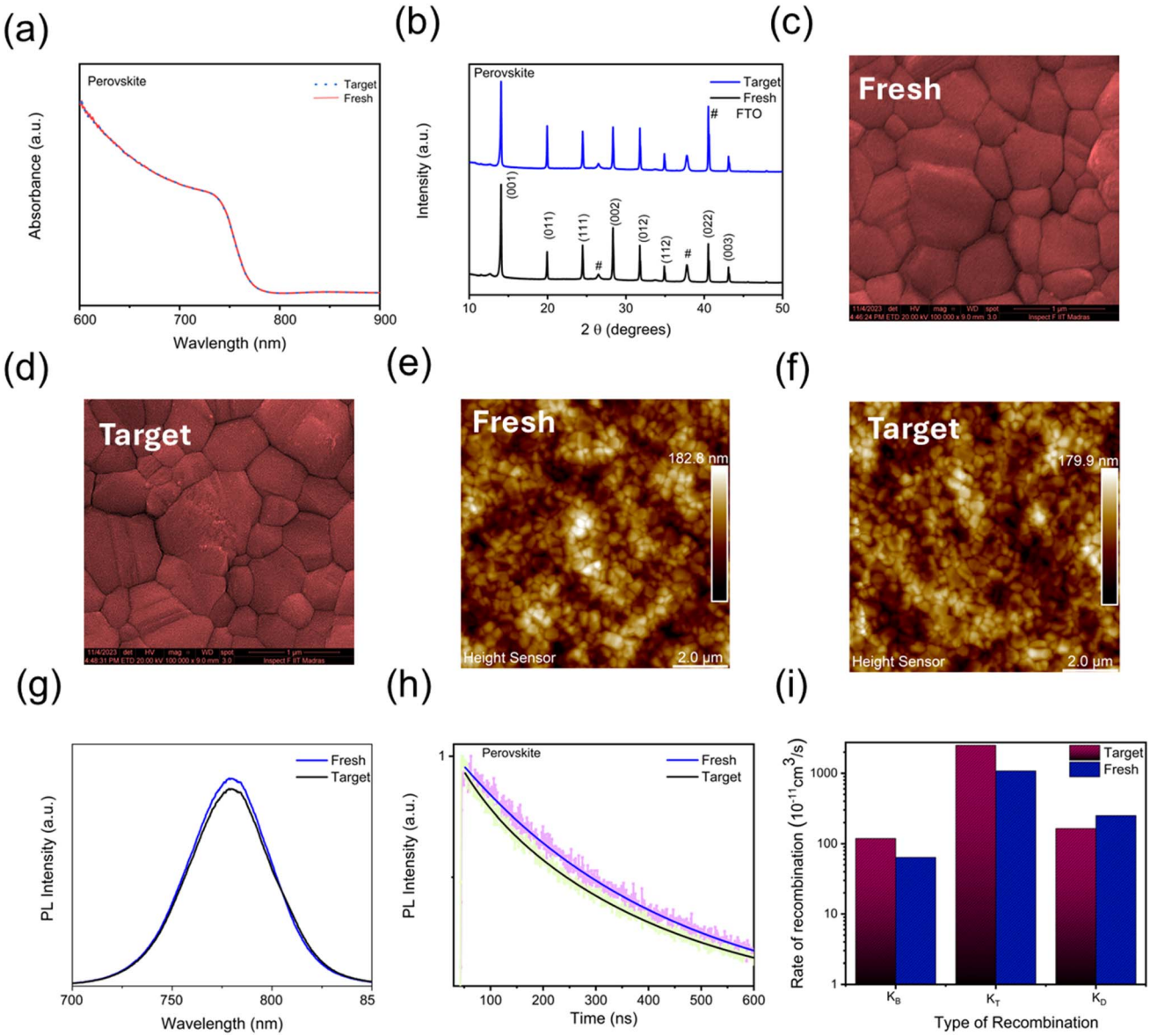

Fig. 4 Characterization of perovskite films on fresh and target substrates. (a) Optical absorption spectra (600–900 nm) of perovskite films. (b) XRD patterns showing the crystalline structure of perovskite materials on fresh and target substrates. (c and d) SEM images of perovskite film morphology on (c) fresh and (d) target substrates (500 nm scale bars). (e and f) 2D AFM topographical images (2.0 µm × 2.0 µm) of perovskite films on (e) fresh substrate and (f) target substrate. (g) Steady-state PL spectra peaks for both substrates. (h) TRPL decay curves for perovskite films. (i) Bar chart showing recombination rate constants (K_B, K_T, and K_D) extracted from time-resolved photoluminescence (TRPL) fitting for both sample types.

(001), (011), (111), (002), (012), (112), (022), and (003), which are consistent with a pseudocubic structure. The absence of significant peaks at around 11.7° (which would indicate optically inactive δ-$FAPbI_3$) and minimal presence of peaks at 12.7° (which would indicate excess PbI_2) suggest high phase purity in these samples.[73] This confirms the successful formation of the desired perovskite phase with minimal impurities. Fresh samples showed a microstrain of magnitude 9.11×10^{-4}, while the target sample showed a microstrain of 0.10×10^{-4}, as calculated using the Williamson–Hall analysis, as shown in Fig. S8a. Similar patterns show preserved crystal structures of perovskite in fresh and target samples. Fig. 4c and d show the SEM images of perovskite coated on fresh and target substrates. Both surfaces show a uniform, densely packed crystalline structure with well-defined grain boundaries similar to the fresh substrate, indicating that the morphology of the perovskite crystals is reproduced on the target surbstrate.[74] Fig. 4e is a 2D AFM image of the perovskite on the fresh substrate with the R_q measured at 26 nm. The relatively low roughness indicates a smooth surface, which signifies the formation of high-quality perovskite films.[75,76] Fig. 4f is a 2D AFM image of the perovskite on the target substrate with R_q being slightly higher at 27 nm. Other AFM statistical parameters of both perovskite films are given in Table S3.

Open Access Article. Published on 01 October 2025. Downloaded on 1/19/2026 7:04:07 PM.
This article is licensed under a Creative Commons Attribution 3.0 Unported Licence.

The steady-state photoluminescence (PL) spectra in Fig. 4g are presented for perovskite materials on fresh and target samples. The fresh and target perovskite samples exhibit a prominent PL peak with a symmetric profile, characteristic of the radiative recombination of charge carriers in the perovskite material.[77] The peak position lies in the 750 to 800 nm range for the triple cation perovskite material. The similarity in peak positions suggests that the electronic properties of the perovskite are preserved after the recycling process, radiative recombination is of similar magnitude in both samples, and no other defect peak is detected. Fig. 4h shows the TRPL decay curves for perovskite coated on fresh and target substrates. The decay profiles of the perovskite films on different ETLs are fitted with a double exponential decay function, and the average lifetime τ_{avg} for a system described by double exponential decay is given in the SI. Both samples yield a lifetime of 120–140 ns (fresh sample, 137.8 ± 3.2 ns, and target sample, 122.9 ± 4.3 ns), while Table S4 shows the corresponding fitting parameters. Fig. 4i shows the recombination kinetics of perovskite compositions on fresh and target samples, *via* their fundamental rate constants using the mathematical models developed by Péan *et al.* and an open-source program.[78] The analysis reveals bimolecular recombination constants (K_B) of 1.19×10^{-9} cm^3 s^{-1} for the fresh sample and 0.64×10^{-9} cm^3 s^{-1} for the target sample. These values fall in the expected range for high-quality perovskites.[79] The trapping rate constants (K_T) are 1.06×10^{-8} cm^3 s^{-1} for fresh and 2.05×10^{-8} cm^3 s^{-1} for target samples. The target sample exhibits nearly twice the trapping rate of the fresh sample, suggesting higher defect density. The magnitude of K_T relative to K_B is approximately 9 : 1 for fresh and 32 : 1 for

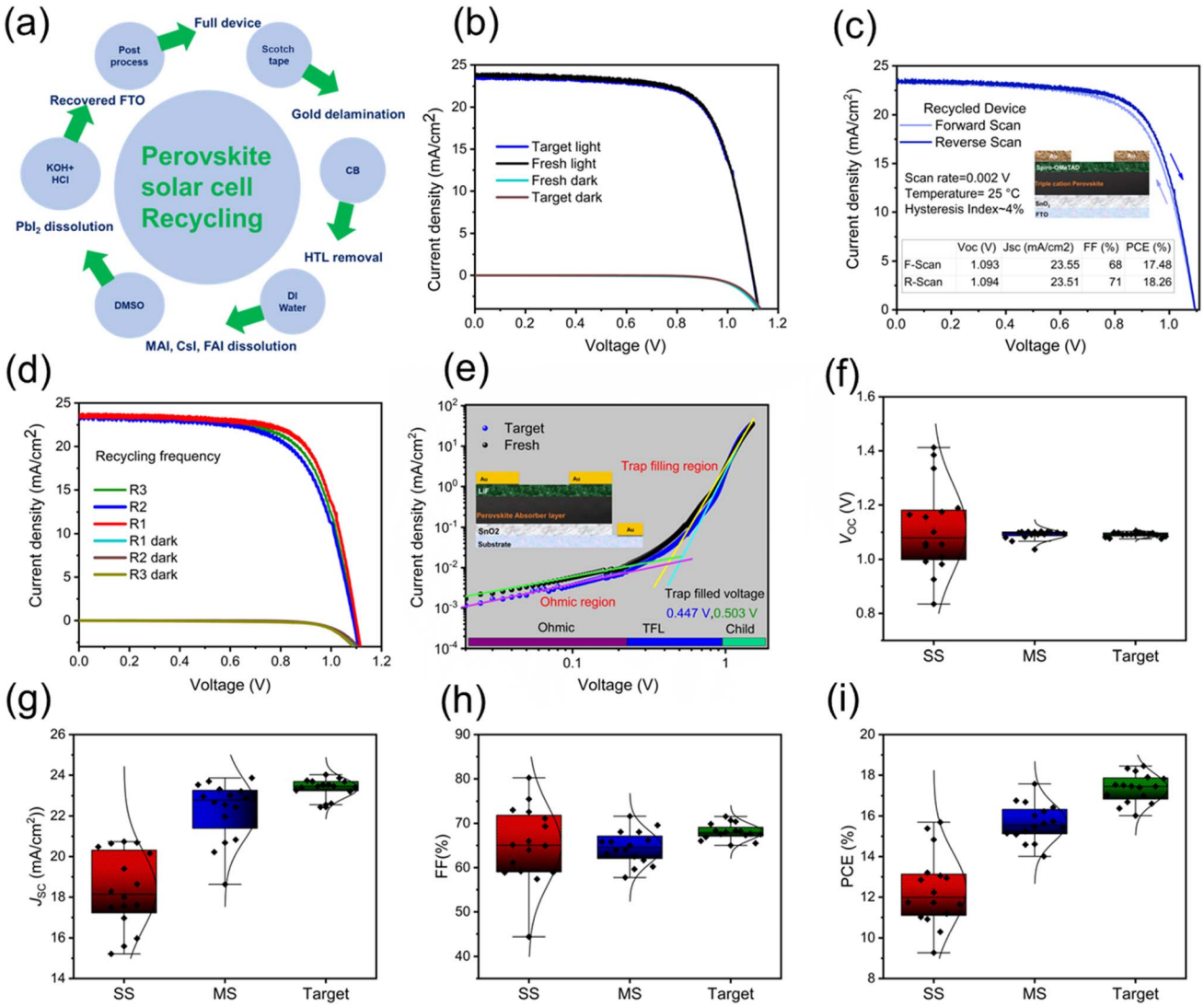

Fig. 5 PSC recycling process and performance characterization. (a) Schematic of PSC recycling workflow showing various stages, including substrate recovery and material extraction. (b) *JV* curves comparing devices fabricated on fresh and target substrates with forward/reverse scans. (c) *JV* characteristics of the device on the target substrate, with performance metrics shown in the inset. (d) *JV* curves after multiple target cycles (R1, R2, and R3). (e) Space-charge-limited current (SCLC) measurements of perovskite electron-only devices on fresh and target substrates. (f–i) Statistical distribution of PV parameters across SS, MS, and target substrates: (f) V_{OC}, (g) J_{SC}, (h) FF, and (i) PCE presented as box plots with individual data points.

 © 2025 The Author(s). Published by the Royal Society of Chemistry

Open Access Article. Published on 01 October 2025. Downloaded on 1/19/2026 7:04:07 PM. This article is licensed under a Creative Commons Attribution 3.0 Unported Licence.

target samples. The de-trapping constants (K_D) of 2.5×10^{-9} $cm^3\ s^{-1}$ (fresh) and 1.65×10^{-9} $cm^3\ s^{-1}$ (target) reveal that the target sample shows a lower de-trapping rate than the fresh sample, indicating a deeper trap state compared to the fresh sample. The $K_T : K_D$ ratio (approximately 4 : 1 for fresh and 12 : 1 for target) provides insight into the trap depth. This increased detrapping in both samples contributes to their improved carrier lifetimes by allowing the re-emission of trapped carriers. Fig. S8b quantifies the relative contributions of each recombination pathway. Trapping accounts for approximately 59% of recombination in the fresh sample *versus* 72% in the target sample. Both samples are consistent with defect-mediated recombination being the primary loss mechanism in halide perovskites, which could explain the smaller device efficiency shown in Fig. 5, in comparison to the recent high-efficiency perovskite solar cells. Bimolecular recombination accounts for approximately 35% in the fresh sample *versus* 27% in the target sample. This shift toward radiative recombination is consistent with the literature finding that high-quality perovskites typically show bimolecular contributions around 30%.[80] The low bimolecular contribution compared to trapping suggests that trap states are not saturated. Detrapping contribution decreases from 6% in the fresh sample to <1% in the target sample. This significant increase in de-trapping indicates modification of trap state energetics.

Performance evaluation of the recycled device

Fig. 5a shows the schematic diagram of the recycling process and reutilization of the substrate for fresh perovskite device fabrication. To understand the utilization of recycled substrates, we fabricated complete PSCs on fresh and target substrates using the device fabrication process described in the Experimental section. Fig. 5b relates the performance of a PSC with fresh and target substrates, and both devices showed similar performances. Fig. 5c shows the *JV* characteristics of a PSC fabricated on a recycled substrate. The inset table shows key performance metrics for the solar cell with open-circuit voltage (V_{OC}) values of 1.093 V (forward scan) and 1.094 V (reverse scan), short-circuit current density (J_{SC}) values of 23.55 mA cm^{-2} (forward scan) and 23.51 mA cm^{-2} (reverse scan), fill factor (FF) values of 68% (forward scan) and 71% (reverse scan), and PCE values of 17.48% (forward scan) and 18.26% (reverse scan). The hysteresis index is approximately 4%, indicating minimal hysteresis between the forward and reverse scans. Fig. 5d shows the *JV* curves for a PSC with substrates recycled multiple times (R1, R2, and R3). The curves are closely grouped, indicating that solar cell performance is maintained even after multiple recycling processes, with device parameters of R1 being the same as in Fig. 5c. This suggests that the recycling protocol is robust and that the substrate can be reused multiple times without substantial loss in efficiency. Fig. S9a presents the dark *JV* curves for fresh and target recycled substrates. The overlap of the curves for both samples indicates that the target recycling process does not adversely affect the recombination processes in the solar cell. Fig. 5e illustrates the V_{TFL} determination for fresh and target substrates, with the inset showing the schematic for an electron-only device. The V_{TFL} shows a slight difference between the fresh (0.447 V) and target substrates (0.503 V), having a slightly higher trap-filled voltage with the trap density of the fresh sample at 1.20×10^{15} cm^{-3} and the target sample at 1.35×10^{15} cm^{-3}, determined using the formula described in the SI.

The statistical analysis of device parameters for PSCs coated on SS, MS, and target substrates is depicted in Fig. 5f–i. The analysis provides insights into the reproducibility and efficiency of devices fabricated on SS, MS, and target substrates. Target devices consistently showed the highest median values for V_{OC}, J_{SC}, and FF. MS devices perform intermediately, while SS devices exhibit the lowest medians. Notably, target substrates demonstrate the tightest distribution across all parameters, indicating superior consistency. In contrast, SS substrates show the broadest data spread, reflecting greater performance variability. These results confirm that target devices achieve higher performance values and better consistency, essential for reliable device operation. Fig. S9b shows that the target substrate devices exhibit the highest shunt resistance (R_{sh}), indicating minimal leakage current paths compared to MS and SS substrates. Fig. S9c reveals that the target configuration also achieves the lowest series resistance (R_s), demonstrating reduced resistive losses.[81]

Techno-economic impact of recycling for perovskite PV technology

To assess the technoeconomic potential, we assumed a 100 MW utility-scale power plant operating under a power purchase agreement, with module efficiency ranging from 16% to 22%. Fig. S10 shows the assembly line schematic for the sequential manufacturing process from the front glass substrate through ITO sputtering, three scribing steps (P1, P2, and P3), deposition of functional layers (SnO_2, perovskite, and spiro-OMeTAD), metal electrode application, testing, sealing, and final assembly, culminating in the completed photovoltaic device for perovskite module fabrication. The system has a DC-to-AC ratio of 1.4 (defined in the SI), a system lifetime between 5 and 30 years, and degradation rates between 0.5% and 5%. Additional details, including yearlong weather data specific to the location (Fig. S11a and b), technical module parameters, manufacturing equipment specifications, utility-scale solar installation parameters, technical central inverter parameters, cost breakdown of modules, various financial assumptions, and DC and AC power losses, are provided in Tables S5–S12. Various module component costs, such as glass, ITO, and others, were removed during the cost calculation of the recycled module compared to the fresh module. The levelized cost of electricity (LCOE) calculations were conducted using the System Advisor Model developed by the National Renewable Energy Laboratory, USA.[82] The LCOE across different solar cell technologies offers valuable insights into economic feasibility and competitiveness. Fig. 6a shows the pie chart breakdown of the cost contributions of various components used in PSC modules. Notably, the junction box accounts for 23.67%, followed by the front glass at 22.09%. The hole transport material, spiro-OMeTAD, also

Open Access Article. Published on 01 October 2025. Downloaded on 1/19/2026 7:04:07 PM.
This article is licensed under a Creative Commons Attribution 3.0 Unported Licence.

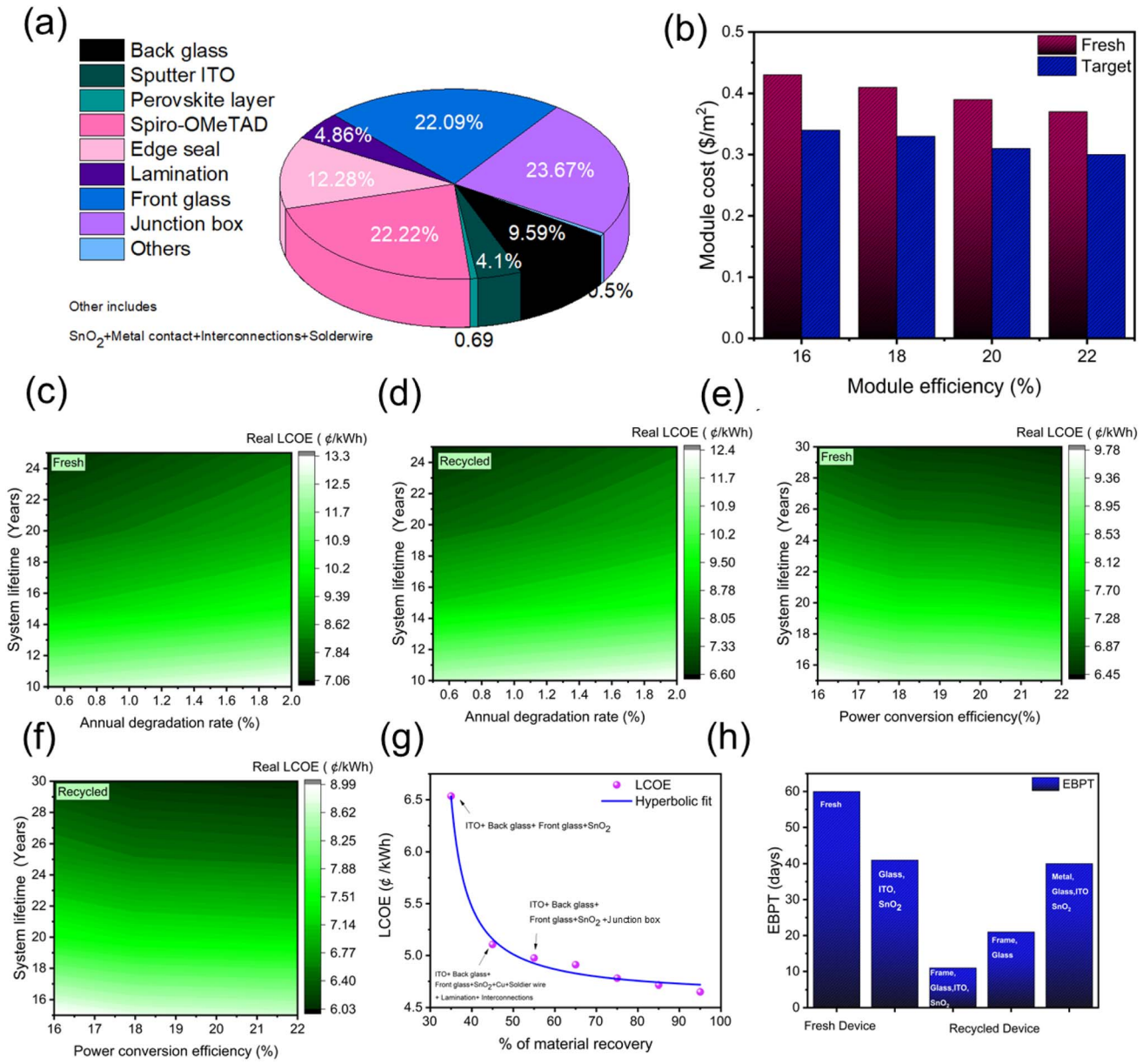

Fig. 6 Techno-economic analysis of perovskite modules: (a) cost distribution of perovskite solar module components.[5,83] (b) Module cost ($ per m^2) comparison between fresh and recycled perovskite modules at 35% material recovery across varying efficiencies (16–22%). (c–f) Real LCOE ($ per kWh) dependence on annual degradation rate, PCE, and material recovery for fresh and recycled modules. (g) LCOE reduction trend with increasing material recovery percentages. (h) EPBT for perovskite modules with different component recovery scenarios.

constitutes a huge portion at 22.22%. The edge seal (12.28%) and back glass (9.59%) further add to the overall costs, while lamination (4.86%) and sputter ITO (4.1%) represent smaller but still notable fractions. Interestingly, the active perovskite layer contributes only 0.5% of the total cost, underscoring its material efficiency and low expense relative to other components. Additional elements such as SnO_2, metal contacts, interconnections, and solder wire collectively account for only 0.69%, classified under 'others'. The bar chart in Fig. 6b illustrates a systematic comparison between fresh perovskite modules and their recycled counterparts across multiple PCE benchmarks (16%, 18%, 20%, and 22%), revealing consistent cost reductions achieved when glass substrates (front glass + back glass + ITO + SnO_2) are recovered and reintegrated into manufacturing processes. At 16% module efficiency, fresh perovskite modules demonstrate a manufacturing cost of approximately \$0.42 m^{-2}, while recycled modules utilizing recovered glass/FTO/SnO_2 substrates achieve a reduced cost of \$0.34 m^{-2}, representing a 19% cost reduction. This economic advantage persists across all efficiency tiers. The cost differential becomes increasingly pronounced at higher efficiency levels, with 20% of efficient modules exhibiting costs of \$0.39 m^{-2} (fresh) *versus* \$0.30 m^{-2} (recycled) and 22% of efficient modules achieving \$0.37 m^{-2} (fresh) compared to \$0.29 m^{-2}

 © 2025 The Author(s). Published by the Royal Society of Chemistry

Open Access Article. Published on 01 October 2025. Downloaded on 1/19/2026 7:04:07 PM.
This article is licensed under a Creative Commons Attribution 3.0 Unported Licence.

(recycled). The economic rationale for substrate recycling becomes particularly evident when examining the cost distribution illustrated in the companion pie chart, which reveals that front glass (22.09%), back glass (9.59%), and related components collectively constitute approximately 31.68% of total module manufacturing expenses. Manufacturers can reduce material input costs without compromising performance characteristics by recovering and reusing these high-value components. Notably, our recycling process maintains the functional integrity of these components, preserving key optoelectronic properties while eliminating the energy-intensive manufacturing steps required for new component production compared with other PV recycling technologies such as silicon, CdTe, *etc*.[16,17,20] The economic benefits quantified here represent only direct material cost reductions and underestimate the comprehensive advantages of recycling strategies, including reduced energy inputs and decreased waste management expenses.[4] Fig. 6c–f present a comparative analysis of the real LCOE for fresh and recycled PV perovskite modules under varying operational parameters, while Fig. S12a–d show the nominal LCOE data with similar input parameters. Fig. S13 shows the annual energy production per year for a module efficiency of 22%, an annual degradation rate of 0.5%, and a system lifetime of 30 years. These contour maps visualize the economic implications of different system lifetimes, degradation rates, and PCEs on the cost-effectiveness of solar energy production using perovskite modules. Fig. 6c illustrates the real LCOE (₵ per kWh) for fresh PV modules as a function of system lifetime (10–25 years) and annual degradation rate (0.5–2.0%). The LCOE values range from 7.06 to 13.3 ₵ per kWh, with the highest value at low system lifetimes (10–12 years). As the system lifetime increases beyond 15 years, LCOE values decrease significantly, reaching optimal values between 7 and 9 ₵ per kWh at higher lifetimes and lower degradation rates. However, a 5% annual degradation rate dramatically increases the LCOE for perovskite-based modules from an initial 7.06 ₵ per kWh to 23.86 ₵ per kWh, which represents more than 3.5 times increase in LCOE, severely undermining the technology's economic competitiveness. Fig. S14a and b show system-generated annual energy production decline over a 5-year period and depict various energy loss mechanisms. Thus, for perovskite technology to meet current industry warranty requirements, annual degradation rates must be below 5%. The contour map in Fig. 6d shows the real LCOE for recycled PV modules under identical parameter ranges. The LCOE values span from 6.60 to 12.4 ₵ per kWh, consistently lower than fresh modules under equivalent conditions. This demonstrates the economic advantage of recycled modules, with optimal performance achieved at higher system lifetimes and lower degradation rates. The contour map in Fig. 6e examines the fresh module LCOE as a function of PCE (16–22%) and system lifetime (15–30 years). LCOE values range from 6.45 to 9.78 ₵ per kWh, with the lowest costs achieved at high efficiency (21–22%) and extended lifetime (28–30 years) combinations. The steep gradient in the green region (16–18 years) indicates that extending the system lifetime beyond this threshold delivers significant economic benefits, especially when coupled with higher PCE. Recycled modules consistently demonstrate lower LCOE values (0.4–0.9 ₵ per kWh reduction) compared to fresh modules under identical operational conditions, as shown in Fig. 6f. System lifetime emerges as the most influential parameter affecting the LCOE, with dramatic cost reductions observed when extending operational lifespans beyond 16 years for both module types. Annual degradation rates below 1% improve economic performance, particularly for systems with longer operational lifetimes. PCE demonstrates a notable but less dramatic impact on the LCOE than the system lifetime. Fig. 6g shows a pronounced negative correlation between the percentage of material recovery and the resulting LCOE. Data fitting was achieved using a hyperbola fit, $Y = \frac{A}{(X-B)} + C$, and the values of fitting parameters were obtained as $A = 8$, $B = 30.87$, and $C = 4.59$. A steep decline in the LCOE occurs as material recovery increases from 30% to approximately 45%, where the LCOE drops to about 5.1₵ per kWh, representing a reduction of 22%. Beyond 45% recovery, the LCOE continues to decrease, though at a more gradual rate, following a near-linear trend through the 50–95% recovery range. At 95% material recovery, the LCOE reaches its minimum value of approximately 4.6 ₵ per kWh, representing a total reduction of nearly 30% compared to the 30% recovery scenario. The findings indicate that research and development efforts should focus on advancing recovery rates from low (30%) to moderate levels (45–50%), as this range captures the steepest segment of the economic benefit curve. The inset summarizes key module material recovery components: a 35% recovery rate corresponds to the reclamation of ITO, SnO_2, front glass, and back glass, while a 45% recovery rate includes additional materials such as Cu, interconnections, and solder wire lamination. Fig. 6h illustrates the energy payback time (EBPT) for fresh and recycled perovskite modules with varying levels of component recovery. Table S13 shows the primary energy demand for various components of the perovskite module. The fresh device exhibits the highest EBPT, approximately 60 days, indicating the longest time required to recover the energy invested in its production. In contrast, recycled devices show significantly reduced EBPT values depending on the components recovered. When only the frame, glass, ITO, and SnO_2 are recovered, the EBPT drops dramatically to around 10 days, representing the most energy-efficient recovery scenario. Recovering just the frame and glass results in a moderate EBPT of about 20 days, while recovering metal along with glass, ITO, and SnO_2 leads to an EBPT close to 40 days. Fig. 7 shows the scatter plot comparing LCOE values (₵ per kWh) with PCE% for various solar cell technologies published in the literature. PSCs exhibit a wide range of PCE values, from approximately 16% to 25%, with corresponding LCOE values ranging from 3 ₵ per kWh to 14.5 ₵ per kWh. This variability reflects ongoing advancements in perovskite technology and its potential for achieving high efficiency and competitive electricity costs. Silicon solar cells show a similar range of efficiencies (15–28%) but tend to achieve lower LCOE values between 3 ₵ per kWh and 8 ₵ per kWh due to their mature manufacturing processes and widespread adoption. CIGS (Copper Indium Gallium Selenide)

Open Access Article. Published on 01 October 2025. Downloaded on 1/19/2026 7:04:07 PM.
This article is licensed under a Creative Commons Attribution 3.0 Unported Licence.

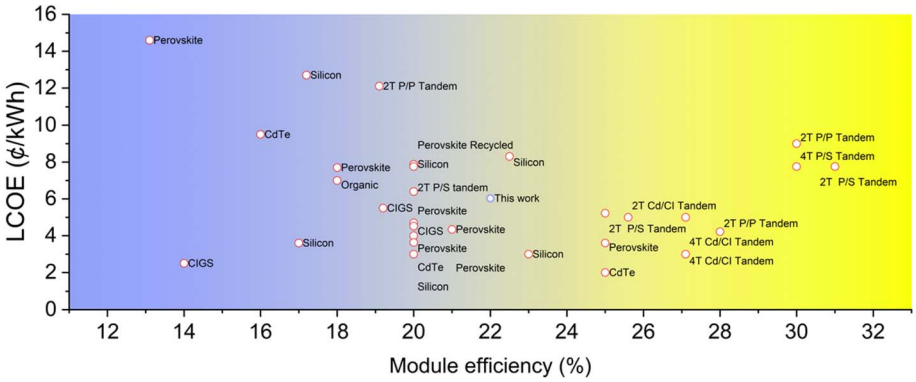

Fig. 7 LCOE *vs.* module efficiency comparison across various PV technologies published in the literature, with LCOE data collected from ref. 84–104.

technology demonstrates PCE values between approximately 14% and 20%, with LCOE values ranging from 2.5 ¢ per kWh to 5.5 ¢ per kWh, indicating strong economic performance in certain applications. Tandem configurations involving perovskite layers exhibit promising results. Two-terminal perovskite–perovskite (2T P/P) tandems achieve ∼12 ¢ per kWh at ∼15% PCE, while two-terminal perovskite–silicon (2T P/S) tandems reach ∼5–6 ¢ per kWh at efficiencies exceeding 27%. Four-terminal cadmium telluride/CIGS tandems (4T CdCI) demonstrate even lower LCOE values (∼4–5 ¢ per kWh) at similar high efficiencies (∼26–28%). Cadmium telluride (CdTe) technologies show varying performance metrics across LCOE values (∼2–9 ¢ per kWh), reflecting their adaptability in different market segments. The scatter plot underscores that while standalone perovskite cells are competitive, tandem configurations combining perovskites with silicon or other materials can achieve superior efficiency and lower electricity costs, making them highly attractive for commercial deployment.

Conclusions

The persistent challenge of residual impurities in end-of-life perovskite solar cells presents a significant barrier to effective recycling and reproducible device fabrication. In this study, we systematically characterized the residual signatures left by two prevalent recycling protocols, the SS and MS methods, following perovskite layer dissolution. Advanced surface and compositional analyses revealed that both approaches leave behind trace contaminants, notably C, Cs, and Pb, which compromise substrate quality and limit their reuse in high-efficiency PSCs. To address these limitations, we implemented a novel post-treatment protocol that substantially reduces residual impurities, enabling the recovery of EOL substrates to a near-pristine state. Devices fabricated on these post-treated substrates demonstrated highly reproducible performance, with a power conversion efficiency variation of just 2.5% across 16 devices, in stark contrast to the 6% variation observed with conventional SS recycling. This clear correlation between impurity removal and device performance underscores the critical importance of targeted post-treatment for reliable PSC fabrication. Our comprehensive techno-economic analysis further highlights the substantial benefits of this recycling methodology. Specifically, the approach yields reductions in the levelized cost of electricity (by 0.4 to 0.9 ¢ per kWh) and energy payback time (by 20 to 40 days) for utility-scale PSC installations. These gains are most pronounced in scenarios featuring high device efficiency, extended operational lifetimes, or reduced degradation rates. Moreover, component-specific recovery, such as glass, ITO, junction boxes, and metal frames, delivers additional economic advantages, reinforcing the value proposition of advanced recycling. Collectively, this work establishes a robust, experimentally validated framework for the high-yield, economically viable, and environmentally responsible recycling of PSCs. The findings advance the field toward sustainable large-scale deployment of perovskite photovoltaics by integrating innovative recycling protocols with rigorous techno-economic validation. Future scope of this work involves investigating alternative chemical methods for gentle removal to eliminate residual impurities without harming the underlying substrate, examining the impact of the proposed protocol on different architectures of perovskite solar cells, and addressing challenges linked to encapsulation removal in perovskite devices and modules.

Experimental section

Chemicals

The chemicals used in this study were used as received from the company without further purification. 15% tin(IV) oxide in H_2O colloidal dispersion was purchased from Alfa Aesar. Hellmanex soap and spiro-OMeTAD (99%) were purchased from Sigma-Aldrich. Trimethylpropylammonium bis(trifluoromethanesulfonyl)imide (98%), lead iodide (PbI_2) (99.99%), formamidinium iodide (FAI) (99.99%), methylammonium bromide (MABr) (98.0%), lead bromide ($PbBr_2$) (98.0%), cesium iodide (CsI) (99.0%), 4-*tert*-butylpyridine (96.0%), and lithium bis(trifluoromethanesulfonyl)imide (98.0%) were purchased from Tokyo Chemical Industry (TCI). Isopropanol (99.5%), acetone (99.5%), dimethyl sulfoxide (DMSO) (99.0%), *N*,*N*-dimethylformamide (DMF) (99.5%),

 © 2025 The Author(s). Published by the Royal Society of Chemistry

Open Access Article. Published on 01 October 2025. Downloaded on 1/19/2026 7:04:07 PM.
This article is licensed under a Creative Commons Attribution 3.0 Unported Licence.

acetonitrile (ACN) (99%), and chlorobenzene (CB) (99.5%) were purchased from Merck. 2.2 mm-thick FTO-coated glass plates with 15 Ω per square sheet resistance were purchased from Greatcell Solar Materials. HCl (37% by weight), KOH (pellets, 99.99%), and KCl (pellets, 99.5%) were purchased from Sigma-Aldrich.

Device fabrication

All the devices and films for characterization were fabricated under air ambient conditions with controlled humidity (25% RH). FTO glass substrates (TEC-15) of 2.5 × 2.5 cm^2 area were cleaned thoroughly with detergent (2% Hellmanex in DI water), acetone, and isopropyl alcohol (IPA) by ultrasonication for 30 minutes each. The nitrogen dried FTO substrates were further treated with UV-ozone cleaning for 20 minutes. A thin layer of SnO_2 film was spin-coated on the cleaned FTO substrates. 15% tin(IV) oxide in H_2O colloidal solution was diluted 1 : 5 V/V in DI water for the deposition. The prepared solution was sonicated for 30 minutes, followed by stirring for 10 minutes at 600 rpm. Then, 150 mL of solution was used to deposit each SnO_2 layer, spinning at 3000 rpm (rotations per minute) for 30 seconds. Then, SnO_2 spin-coated substrates were dried at 120 °C for 60 minutes. The perovskite substrate was pre-treated using 30 mM KCl salt dissolved in DI water and post-dried at 120 °C. The FA/MA/Cs perovskite films were spin-coated from a precursor solution containing FAI (1 M), PbI_2 (1.1 M), MABr (0.2 M), and $PbBr_2$ (0.2 M) in anhydrous DMF : DMSO (4 : 1 (v/v)) with CsI (1.5 M, with the desired amount in DMSO). The Cs/FA/MA solution was vigorously stirred at 810 rpm at 65 °C for 60 min, then 80 μL of this solution was dropped on the substrate and spin-coated at 0 rpm for 5 s, then 1200 rpm for 12 s, and the spin rate was accelerated to 6000 rpm for 30 s. Antisolvents were dripped at the 23rd second. After spin coating of the precursor solution, the substrates were transferred to the hot plate and heated at 102 °C for 60 min. The perovskite substrates were covered with a glass Petri dish in all cases. After cooling down to 60 °C, the spiro-OMeTAD hole transport layer (HTL) was spin-coated on top of the perovskite film at 2000 rpm for 30 s from an 8 wt% solution of spiro-OMeTAD in chlorobenzene solution containing additives of 24.66 μL lithium bis(trifluoromethanesulfonyl)imide and 5.75 μL 4-*tert*-butylpyridine. Before metal coating, all the samples were kept overnight for ageing in a dry room. Finally, an Au metal electrode of about 100 nm was thermally evaporated on top of the spiro-OMeTAD layer. Various samples deposited on the fresh substrate FTO/SnO_2 are termed 'fresh' throughout the manuscript. Devices were fabricated on a recycled substrate by repeating the same protocol as described above. For an electron-only device, a LiF layer of a few nm was deposited using thermal evaporation.

Process of recycling

Single solvent (SS) recycling process. The end-of-life perovskite solar cells were processed to recycle FTO substrates by peeling off the gold electrode using Scotch tape. The remaining device layers were dissolved in DMSO solvent. Recovered substrates underwent cleaning with DI water, acetone, IPA, and UV-ozone (UVO) treatment before reuse in perovskite device fabrication. These substrates are labelled as 'SS' in the manuscript.

Multi-solvent (MS) recycling process. The gold electrode was delaminated using ethyl acetate. Subsequent steps included dissolving the HTL in chlorobenzene (CB) with 10-minute sonication, removing MAI, FAI, and CsI *via* DI water sonication (10 minutes), and dissolving PbI_2 residues with DMSO. Recovered substrates were cleaned with DI water, acetone, IPA, and UVO treatment. These substrates are labelled as 'MS' throughout the manuscript.

Target recycling process. This method follows the MS recycling steps for gold delamination, HTL dissolution, cation removal, and PbI_2 dissolution until substrates with high residual impurities are recovered. The cleaning protocol was enhanced by adding sequential treatments with potassium hydroxide (KOH, 0.5–0.9 M in DI water) to neutralize organic residues, rinse with DI water, followed by an acid wash using hydrochloric acid (HCl, 37%, diluted 1 : 8 v/v in DI water) and further rinse with DI water to eliminate inorganic traces. After rinsing with DI water, substrates underwent UVO treatment. This improved the surface properties for subsequent perovskite device fabrication. Standardized UVO treatment across all samples ensured that any observed differences in contact angles across different samples are primarily attributable to the presence of residual impurities and their effects on surface affinity for perovskite precursors, rather than variations in surface oxidation states caused by differential UVO exposure.

Device characterization. Morphological, structural, and optical characterization experiments were performed using a scanning electron microscope (Zeiss MERLIN), an X-ray diffractometer (D8 Discover, Bruker) with a Cu Kα radiation source, and a UV-Vis spectrometer (UV-1800, Shimadzu), respectively. Topographical analysis was conducted with an Agilent 5500 atomic force microscope (AFM). Photoluminescence measurements were carried out using a Horiba iHR 320 spectrometer, while time-resolved photoluminescence (TRPL) was measured with a Horiba Fluorolog-QM Microspectrometer. Contact angle measurements were performed using a DataPhysics goniometer (Model OCA 15 Pr) with a droplet volume of 10 μL, and X-ray photoelectron spectroscopy (XPS) was conducted with a PHI 5000 VersaProbe III system. Device performance was evaluated under ambient conditions (relative humidity, 15–85%), with devices stored after measurement in a humidity-controlled dry room (15–40% RH) and covered with aluminium foil. Photovoltaic measurements were performed under simulated AM 1.5G illumination, 100 mW cm^{-2}, provided by a PEC-L01 solar simulator from Peccell Technologies. Current–voltage (*J*–*V*) characteristics for devices with an active area of 0.09 cm^2 were measured using a Keithley 2450 Source Measure Unit, and dark *J*–*V* measurements were conducted over a voltage range of −1.5 to 1.5 V at a scan rate of 20 mV s^{-1}.

Author contributions

DK, JKR, and TS contributed to the conception and design of the study. DK performed the experiments and processed the data

Open Access Article. Published on 01 October 2025. Downloaded on 1/19/2026 7:04:07 PM.
This article is licensed under a Creative Commons Attribution 3.0 Unported Licence.

under the supervision of JKR and TS. YGN assisted in techno-economic analysis and techno-economic data collection. DK, JKR, and TS contributed to manuscript writing. TS and JKR supervised the project.

Conflicts of interest

There are no conflicts to declare.

Data availability

The data supporting this article have been included as part of the supplementary information (SI). Supplementary information: supporting figures showing step-by-step recycling processes, cross-sectional device images, EDX spectra and quantitative analysis, elemental mapping images, 3D AFM images, XRD data, XPS survey scans, Williamson-Hall analysis, dark *J–V* characteristics, device performance statistics, TRPL fitting equations and parameters, environmental impact calculations, solar irradiance profiles, manufacturing cost breakdowns, financial analysis tables, energy production modeling, and detailed experimental procedures have been included as part of the SI. See DOI: **https://doi.org/10.1039/d5el00131e**.

Acknowledgements

DK gratefully acknowledges the Ministry of Education, Government of India, for providing support through the Prime Minister's Research Fellowship (PMRF). JKR is acknowledged for providing experimental characterization facilities and TS for support with device fabrication and characterization. YGN acknowledges DK and JKR for the technoeconomic problem conceptualization and simulation data generation. JKR acknowledges DST for some of the experimental facilities within the DSEHC project. TS acknowledges the Anusandhan National Research Foundation (ANRF) for providing financial support under the CRG grant (CRG/2023/003135) and IIT Delhi for providing infrastructural facilities.

References

1 R. G. Charles, A. Doolin, R. García-Rodríguez, K. V. Villalobos and M. L. Davies, Circular economy for perovskite solar cells – drivers, progress and challenges, *Energy Environ. Sci.*, 2023, **16**, 3711–3733.
2 X. Tian, S. D. Stranks and F. You, Life cycle assessment of recycling strategies for perovskite photovoltaic modules, *Nat Sustainability*, 2021, **4**(4), 821–829.
3 J. M. Kadro, N. Pellet, F. Giordano, A. Ulianov, O. Müntener, J. Maier, M. Grätzel and A. Hagfeldt, Proof-of-concept for facile perovskite solar cell recycling, *Energy Environ. Sci.*, 2016, **9**, 3172–3179.
4 J. H. Martínez, S. Romero, J. J. Ramasco and E. Estrada, The world-wide waste web, *Nat. Commun.*, 2022, **13**(1), 1–13.
5 X. Xiao, N. Xu, X. Tian, T. Zhang, B. Wang, X. Wang, Y. Xian, C. Lu, X. Ou, Y. Yan, L. Sun, F. You and F. Gao, Aqueous-based recycling of perovskite photovoltaics, *Nature*, 2025, **638**, 670–675.
6 J. Zhou, L. Tan, Y. Liu, H. Li, X. Liu, M. Li, S. Wang, Y. Zhang, C. Jiang, R. Hua, W. Tress, S. Meloni and C. Yi, Highly efficient and stable perovskite solar cells via a multifunctional hole transporting material, *Joule*, 2024, **8**, 1691–1706.
7 T. Rodríguez, S. Vázquez, R. Valdés, I. Rodríguez, P. Figueroa, P. García, C. Castelló, Á. Méndez, A. Photovoltaic Glass Waste, K. Treviño Rodríguez, A. Iriana Sánchez Vázquez, J. Jacobo Ruiz Valdés, J. Ibarra Rodríguez, M. Guadalupe Paredes Figueroa, S. Porcar García, J. Bautista Carda Castelló and A. Álvarez Méndez, Photovoltaic Glass Waste Recycling in the Development of Glass Substrates for Photovoltaic Applications, *Materials*, 2023, **16**, 2848.
8 G. Rodriguez-Garcia, E. Aydin, S. De Wolf, B. Carlson, J. Kellar and I. Celik, Life Cycle Assessment of Coated-Glass Recovery from Perovskite Solar Cells, *ACS Sustain. Chem. Eng.*, 2021, **9**, 15239–15248.
9 A. Binek, M. L. Petrus, N. Huber, H. Bristow, Y. Hu, T. Bein and P. Docampo, Recycling Perovskite Solar Cells to Avoid Lead Waste, *ACS Appl. Mater. Interfaces*, 2016, **8**, 12881–12886.
10 H. Zhang, J. W. Lee, G. Nasti, R. Handy, A. Abate, M. Grätzel and N. G. Park, Lead immobilization for environmentally sustainable perovskite solar cells, *Nature*, 2023, **617**, 687–695.
11 K. Wang, T. Ye, X. Huang, Y. Hou, J. Yoon, D. Yang, X. Hu, X. Jiang, C. Wu, G. Zhou and S. Priya, "One-key-reset" recycling of whole perovskite solar cell, *Matter*, 2021, **4**(7), 2522–2541.
12 B. Augustine, K. Remes, G. S. Lorite, J. Varghese and T. Fabritius, Recycling perovskite solar cells through inexpensive quality recovery and reuse of patterned indium tin oxide and substrates from expired devices by single solvent treatment, *Sol. Energy Mater. Sol. Cells*, 2019, **194**, 74–82.
13 L. Huang, J. Xu, X. Sun, R. Xu, Y. Du, J. Ni, H. Cai, J. Li, Z. Hu and J. Zhang, New Films on Old Substrates: Toward Green and Sustainable Energy Production via Recycling of Functional Components from Degraded Perovskite Solar Cells, *ACS Sustain. Chem. Eng.*, 2017, **5**, 3261–3269.
14 V. Larini, C. Ding, F. Faini, G. Pica, G. Bruni, L. Pancini, S. Cavalli, M. Manzi, M. Degani, R. Pallotta, M. De Bastiani, C.-Q. Ma and G. Grancini, Sustainable and circular management of perovskite solar cells via green recycling of electron transport layer-coated transparent conductive oxide, *Adv. Funct. Mater.*, 2024, **34**(50), 2306040.
15 Z. Ngagoum Ndalloka, H. Vijayakumar Nair, S. Alpert and C. Schmid, Solar photovoltaic recycling strategies, *Sol. Energy*, 2024, **270**, 112379.
16 G. A. Heath, T. J. Silverman, M. Kempe, M. Deceglie, D. Ravikumar, T. Remo, H. Cui, P. Sinha, C. Libby, S. Shaw, K. Komoto, K. Wambach, E. Butler, T. Barnes and A. Wade, Research and development priorities for

 © 2025 The Author(s). Published by the Royal Society of Chemistry

Open Access Article. Published on 01 October 2025. Downloaded on 1/19/2026 7:04:07 PM.
This article is licensed under a Creative Commons Attribution 3.0 Unported Licence.

silicon photovoltaic module recycling to support a circular economy, *Nat. Energy*, 2020, 502–510.

17 D. J. Bradwell, S. Osswald, W. Wei, S. A. Barriga, G. Ceder and D. R. Sadoway, Recycling ZnTe, CdTe, and other compound semiconductors by ambipolar electrolysis, *J. Am. Chem. Soc.*, 2011, **133**, 19971–19975.

18 T. Maani, I. Celik, M. J. Heben, R. J. Ellingson and D. Apul, Environmental impacts of recycling crystalline silicon (c-SI) and cadmium telluride (CDTE) solar panels, *Sci. Total Environ.*, 2020, **735**, 138827.

19 M. Marwede and A. Reller, Future recycling flows of tellurium from cadmium telluride photovoltaic waste, *Resour., Conserv. Recycl.*, 2012, **69**, 35–49.

20 D. Ravikumar, T. Seager, P. Sinha, M. P. Fraser, S. Reed, E. Harmon and A. Power, Environmentally improved CdTe photovoltaic recycling through novel technologies and facility location strategies, *Prog. Photovoltaics Res. Appl.*, 2020, **28**, 887–898.

21 X. Zhang, W. Xu, S. Wang, D. Liu, P. Deng, J. Deng and W. Jiang, Research Status of Recovery of Tellurium from Cadmium Telluride Photovoltaic Modules, *IOP Conf. Ser. Mater. Sci. Eng.*, 2020, **782**, 022024.

22 Y. S. Zimmermann, C. Niewersch, M. Lenz, Z. Z. Kül, P. F. X. Corvini, A. Schäffer and T. Wintgens, Recycling of indium from CIGS photovoltaic cells: Potential of combining acid-resistant nanofiltration with liquid-liquid extraction, *Environ. Sci. Technol.*, 2014, **48**, 13412–13418.

23 I. Teknetzi, S. Holgersson and B. Ebin, Valuable metal recycling from thin film CIGS solar cells by leaching under mild conditions, *Sol. Energy Mater. Sol. Cells*, 2023, **252**, 112178.

24 Q. Song, L. Zhang, C. Yang and Z. Xu, Novel Electrodeposition Method for Cu-In-Cd-Ga Sequential Separation from Waste Solar Cell: Mechanism, Application, and Environmental Impact Assessment, *Environ. Sci. Technol.*, 2021, **55**, 10724–10733.

25 F. W. Liu, T. M. Cheng, Y. J. Chen, K. C. Yueh, S. Y. Tang, K. Wang, C. L. Wu, H. S. Tsai, Y. J. Yu, C. H. Lai, W. S. Chen and Y. L. Chueh, High-yield recycling and recovery of copper, indium, and gallium from waste copper indium gallium selenide thin-film solar panels, *Sol. Energy Mater. Sol. Cells*, 2022, **241**, 111691.

26 D. Hu, B. Ma, X. Li, Y. Lv, Y. Chen and C. Wang, Innovative and sustainable separation and recovery of valuable metals in spent CIGS materials, *J. Clean. Prod.*, 2022, **350**, 131426.

27 A. M. K. Gustafsson, M. R. S. J. Foreman and C. Ekberg, Recycling of high purity selenium from CIGS solar cell waste materials, *Waste Manage.*, 2014, **34**, 1775–1782.

28 A. Amato and F. Beolchini, End-of-life CIGS photovoltaic panel: A source of secondary indium and gallium, *Prog. Photovoltaics Res. Appl.*, 2019, **27**, 229–236.

29 Y. Hou, E. Aydin, M. De Bastiani, C. Xiao, F. H. Isikgor, D. J. Xue, B. Chen, H. Chen, B. Bahrami, A. H. Chowdhury, A. Johnston, S. W. Baek, Z. Huang, M. Wei, Y. Dong, J. Troughton, R. Jalmood, A. J. Mirabelli, T. G. Allen, E. Van Kerschaver, M. I. Saidaminov, D. Baran, Q. Qiao, K. Zhu, S. De Wolf and E. H. Sargent, Efficient tandem solar cells with solution-processed perovskite on textured crystalline silicon, *Science*, 2020, **367**, 1135–1140.

30 G. Yang, M. Wang, C. Fei, H. Gu, Z. J. Yu, A. Alasfour, Z. C. Holman and J. Huang, Recycling Silicon Bottom Cells from End-of-Life Perovskite-Silicon Tandem Solar Cells, *ACS Energy Lett.*, 2023, **8**, 1639–1644.

31 X. Tian, B. Roose, S. D. Stranks and F. You, Periodic module rejuvenation provides early market entry for circular all-perovskite tandem photovoltaic technologies, *Energy Environ. Sci.*, 2023, **16**, 5551–5567.

32 X. Feng, Q. Guo, J. Xiu, Z. Ying, K. W. Ng, L. Huang, S. Wang, H. Pan, Z. Tang and Z. He, Close-loop recycling of perovskite solar cells through dissolution-recrystallization of perovskite by butylamine, *Cell Rep. Phys. Sci.*, 2021, **2**, 100341.

33 P. Chhillar, B. P. Dhamaniya, V. Dutta and S. K. Pathak, Recycling of Perovskite Films: Route toward Cost-Efficient and Environment-Friendly Perovskite Technology, *ACS Omega*, 2019, **4**, 11880–11887.

34 B. Chen, C. Fei, S. Chen, H. Gu, X. Xiao and J. Huang, Recycling lead and transparent conductors from perovskite solar modules, *Nat. Commun.*, 2021, **12**, 1–10.

35 W. Zhu, W. Chai, D. Chen, H. Xi, D. Chen, J. Chang, J. Zhang, C. Zhang and Y. Hao, Recycling of FTO/TiO2 Substrates: Route toward Simultaneously High-Performance and Cost-Efficient Carbon-Based, All-Inorganic CsPbIBr2 Solar Cells, *ACS Appl. Mater. Interfaces*, 2020, **12**, 4549–4557.

36 X. Feng, S. Wang, Q. Guo, Y. Zhu, J. Xiu, L. Huang, Z. Tang and Z. He, Dialkylamines Driven Two-Step Recovery of NiOx/ITO Substrates for High-Reproducibility Recycling of Perovskite Solar Cells, *J. Phys. Chem. Lett.*, 2021, **12**, 4735–4741.

37 C. G. Poll, G. W. Nelson, D. M. Pickup, A. V. Chadwick, D. J. Riley and D. J. Payne, Electrochemical recycling of lead from hybrid organic–inorganic perovskites using deep eutectic solvents, *Green Chem.*, 2016, **18**, 2946–2955.

38 D. Le Khac, S. Chowdhury, A. Soheil Najm, M. Luengchavanon, A. mebdir Holi, M. Shah Jamal, C. Hua Chia, K. Techato and V. Selvanathan, Efficient laboratory perovskite solar cell recycling with a one-step chemical treatment and recovery of ITO-coated glass substrates, *Sol. Energy*, 2024, **267**, 112214.

39 B. J. Kim, D. H. Kim, S. L. Kwon, S. Y. Park, Z. Li, K. Zhu and H. S. Jung, Selective dissolution of halide perovskites as a step towards recycling solar cells, *Nat. Commun.*, 2016, **7**, 11735.

40 M. S. Chowdhury, K. S. Rahman, V. Selvanathan, A. K. M. Hasan, M. S. Jamal, N. A. Samsudin, M. Akhtaruzzaman, N. Amin and K. Techato, Recovery of FTO coated glass substrate via environment-friendly facile recycling perovskite solar cells, *RSC Adv.*, 2021, **11**, 14534–14541.

41 L. Huang, Z. Hu, J. Xu, X. Sun, Y. Du, J. Ni, H. Cai, J. Li and J. Zhang, Efficient electron-transport layer-free planar perovskite solar cells via recycling the FTO/glass

Open Access Article. Published on 01 October 2025. Downloaded on 1/19/2026 7:04:07 PM.
This article is licensed under a Creative Commons Attribution 3.0 Unported Licence.

substrates from degraded devices, *Sol. Energy Mater. Sol. Cells*, 2016, **152**, 118–124.
42 H. J. Kim, O. Y. Gong, Y. J. Kim, G. W. Yoon, G. S. Han, H. Shin and H. S. Jung, Environmentally Viable Solvent Management in Perovskite Solar Cell Recycling Process, *ACS Energy Lett.*, 2023, **8**, 4330–4337.
43 R. Vidal, J. A. Alberola-Borràs, S. N. Habisreutinger, J. L. Gimeno-Molina, D. T. Moore, T. H. Schloemer, I. Mora-Seró, J. J. Berry and J. M. Luther, Assessing health and environmental impacts of solvents for producing perovskite solar cells, *Nat. Sustainability*, 2020, 277–285.
44 M. V. Gallegos, L. Gil-Escrig, K. P. S. Zanoni, H. J. Bolink and L. C. Damonte, Recycling and reusing ITO substrates from perovskite solar cells: A sustainable perspective, *Sol. Energy Mater. Sol. Cells*, 2024, **277**, 113117.
45 K. Valadez-Villalobos and M. L. Davies, Remanufacturing of perovskite solar cells, *RSC Sustain.*, 2024, **2**, 2057–2068.
46 B. Chen, C. Fei, S. Chen, H. Gu, X. Xiao and J. Huang, Recycling lead and transparent conductors from perovskite solar modules, *Nat. Commun.*, 2021, **12**, 1–10.
47 K. Komoto, J.-S. Lee, J. Zhang, D. Ravikumar, P. Sinha, A. Wade, G. Heath, *End-of-Life Management of Photovoltaic Panels Trends in PV Module Recycling Technologies*, 2018, **https://iea-pvps.org/key-topics/end-of-life-management-of-photovoltaic-panels-trends-in-pv-module-recycling-technologies-by-task-12/**.
48 D. Prat, J. Hayler and A. Wells, A survey of solvent selection guides, *Green Chem.*, 2014, **16**, 4546–4551.
49 H. S. Kim, Y. J. An, J. Il Kwak, H. J. Kim, H. S. Jung and N. G. Park, Sustainable Green Process for Environmentally Viable Perovskite Solar Cells, *ACS Energy Lett.*, 2022, **7**, 1154–1177.
50 B. Chen, C. Fei, S. Chen, H. Gu, X. Xiao and J. Huang, Recycling lead and transparent conductors from perovskite solar modules, *Nat. Commun.*, 2021, **12**, 1–10.
51 X. Xiao, N. Xu, X. Tian, T. Zhang, B. Wang, X. Wang, Y. Xian, C. Lu, X. Ou, Y. Yan, L. Sun, F. You and F. Gao, Aqueous-based recycling of perovskite photovoltaics, *Nature*, 2025, **638**, 670–675.
52 L. Punathil, K. Mohanasundaram, K. S. Tamilselavan, R. Sathyamurthy and A. J. Chamkha, Recovery of Pure Silicon and Other Materials from Disposed Solar Cells, *Int. J. Photoenergy*, 2021, **2021**, 5530213.
53 T. Y. Wang, J. C. Hsiao and C. H. Du, Recycling of materials from silicon base solar cell module, *Conference Record of the IEEE Photovoltaic Specialists Conference*, 2012, pp. 2355–2358.
54 S. Gao, X. Chen, J. Qu, Y. Guo, H. Shi, F. Pang, L. Guo, X. Qu, D. Wang and H. Yin, Recycling of silicon solar panels through a salt-etching approach, *Nat Sustainability*, 2024, (7), 920–930.
55 M. Peplow, Solar Panels Face Recycling Challenge, *ACS Cent. Sci.*, 2022, **8**, 299–302.
56 X. Li, B. Ma, C. Wang, D. Hu, Y. Lü and Y. Chen, Recycling and recovery of spent copper—indium—gallium—diselenide (CIGS) solar cells: A review, *Int. J. Miner. Metall. Mater.*, 2023, **30**, 989–1002.
57 F. W. Liu, T. M. Cheng, Y. J. Chen, K. C. Yueh, S. Y. Tang, K. Wang, C. L. Wu, H. S. Tsai, Y. J. Yu, C. H. Lai, W. S. Chen and Y. L. Chueh, High-yield recycling and recovery of copper, indium, and gallium from waste copper indium gallium selenide thin-film solar panels, *Sol. Energy Mater. Sol. Cells*, 2022, **241**, 111691.
58 T. Maani, I. Celik, M. J. Heben, R. J. Ellingson and D. Apul, Environmental impacts of recycling crystalline silicon (c-SI) and cadmium telluride (CDTE) solar panels, *Sci. Total Environ.*, 2020, **735**, 138827.
59 S. Preet and S. T. Smith, A comprehensive review on the recycling technology of silicon based photovoltaic solar panels: Challenges and future outlook, *J. Clean. Prod.*, 2024, **448**, 141661.
60 M. Ahmadian-Yazdi, A. Rahimzadeh, Z. Chouqi, Y. Miao and M. Eslamian, Viscosity, surface tension, density and contact angle of selected PbI2, PbCl2 and methylammonium lead halide perovskite solutions used in perovskite solar, *AIP Adv.*, 2018, **8**(2), 025109.
61 H. Tao, H. Wang, Y. Bai, H. Long, H. Zhao, Q. Fu and Z. Ma, Effects of sputtering power of SnO2 electron selective layer on perovskite solar cells, *J. Mater. Sci.: Mater. Electron.*, 2019, **30**, 12036–12043.
62 Q. Zhang, P. Liu, C. Miao, Z. Chen, C. M. Lawrence Wu and C. H. Shek, Formation of orthorhombic SnO2 originated from lattice distortion by Mn-doped tetragonal SnO2, *RSC Adv.*, 2015, **5**, 39285–39290.
63 N. Sivakumar, D. Kumar, R. Maurya, S. Saha, T. Singh and J. K. Rath, Effects of pure and metal chloride-treated SnO2 electron transport layer on air ambient fabricated perovskite solar cells: electrical, optical, and photovoltaic properties, *J. Mater. Sci.: Mater. Electron.*, 2025, **36**, 1–14.
64 L. Grzadziel, M. Krzywiecki, A. Szwajca, A. Sarfraz, G. Genchev and A. Erbe, Detection of intra-band gap defects states in spin-coated sol-gel SnOx nanolayers by photoelectron spectroscopies, *J. Phys. D Appl. Phys.*, 2018, **51**, 315301.
65 P. van der Heide, *X-Ray Photoelectron Spectroscopy: An Introduction to Principles and Practices*, 2011, DOI: **10.1002/9781118162897**.
66 M. Batzill and U. Diebold, The surface and materials science of tin oxide, *Prog. Surf. Sci.*, 2005, **79**, 47–154.
67 M. Kwoka, L. Ottaviano, M. Passacantando, S. Santucci, G. Czempik and J. Szuber, XPS study of the surface chemistry of L-CVD SnO2 thin films after oxidation, *Thin Solid Films*, 2005, **490**, 36–42.
68 H. B. Lee, N. Kumar, M. M. Ovhal, Y. J. Kim, Y. M. Song and J. W. Kang, Dopant-Free, Amorphous–Crystalline Heterophase SnO2 Electron Transport Bilayer Enables >20% Efficiency in Triple-Cation Perovskite Solar Cells, *Adv. Funct. Mater.*, 2020, **30**, 2001559.
69 M. Saliba, T. Matsui, J. Y. Seo, K. Domanski, J. P. Correa-Baena, M. K. Nazeeruddin, S. M. Zakeeruddin, W. Tress, A. Abate, A. Hagfeldt and M. Grätzel, Cesium-containing triple cation perovskite solar cells: improved stability, reproducibility and high efficiency, *Energy Environ. Sci.*, 2016, **9**, 1989–1997.

 © 2025 The Author(s). Published by the Royal Society of Chemistry

Open Access Article. Published on 01 October 2025. Downloaded on 1/19/2026 7:04:07 PM.
This article is licensed under a Creative Commons Attribution 3.0 Unported Licence.

70 T. Singh and T. Miyasaka, Stabilizing the Efficiency Beyond 20% with a Mixed Cation Perovskite Solar Cell Fabricated in Ambient Air under Controlled Humidity, *Adv. Energy Mater.*, 2018, **8**, 1700677.
71 J. Y. Woo, Y. Kim, J. Bae, T. G. Kim, J. W. Kim, D. C. Lee and S. Jeong, Highly Stable Cesium Lead Halide Perovskite Nanocrystals through in Situ Lead Halide Inorganic Passivation, *Chem. Mater.*, 2017, **29**, 7088–7092.
72 F. Ünlü, E. Jung, J. Haddad, A. Kulkarni, S. Öz, H. Choi, T. Fischer, S. Chakraborty, T. Kirchartz and S. Mathur, Understanding the interplay of stability and efficiency in A-site engineered lead halide perovskites, *APL Mater.*, 2020, **8**, 70901.
73 C. A. R. Perini, A. Reddy Pininti, S. Martani, P. Topolovsek, A. Perego, D. Cortecchia, A. Petrozza and M. Caironi, Humidity-robust scalable metal halide perovskite film deposition for photovoltaic applications, *J. Mater. Chem. A*, 2020, **8**, 25283–25289.
74 Q. An, F. Paulus, D. Becker-Koch, C. Cho, Q. Sun, A. Weu, S. Bitton, N. Tessler and Y. Vaynzof, Small grains as recombination hot spots in perovskite solar cells, *Matter*, 2021, **4**, 1683–1701.
75 E. Rezaee, D. Kutsarov, B. Li, J. Bi and S. R. P. Silva, A route towards the fabrication of large-scale and high-quality perovskite films for optoelectronic devices, *Sci. Rep.*, 2022, **12**, 1–11.
76 J. F. Wang, L. Zhu, B. G. Zhao, Y. L. Zhao, J. Song, X. Q. Gu and Y. H. Qiang, Surface engineering of perovskite films for efficient solar cells, *Sci. Rep.*, 2017, **7**, 14478.
77 D. Kumar, S. Porwal and T. Singh, Role of defects in organic–inorganic metal halide perovskite: detection and remediation for solar cell applications, *Emerg. Mater.*, 2021, **5**(5), 987–1020.
78 E. V. Péan and M. L. Davies, PEARS: A Web Tool for Fitting Time-Resolved Photoluminescence Decays of Perovskite Materials, *J. Chem. Inf. Model.*, 2023, **63**, 4477–4482.
79 M. B. Johnston and L. M. Herz, Hybrid Perovskites for Photovoltaics: Charge-Carrier Recombination, Diffusion, and Radiative Efficiencies, *Acc. Chem. Res.*, 2016, **49**, 146–154.
80 D. W. Dequilettes, S. Koch, S. Burke, R. K. Paranji, A. J. Shropshire, M. E. Ziffer and D. S. Ginger, Photoluminescence Lifetimes Exceeding 8 μs and Quantum Yields Exceeding 30% in Hybrid Perovskite Thin Films by Ligand Passivation, *ACS Energy Lett.*, 2016, **1**, 438–444.
81 R. Singh, S. Sandhu and J. J. Lee, Elucidating the effect of shunt losses on the performance of mesoporous perovskite solar cells, *Sol. Energy*, 2019, **193**, 956–961.
82 System Advisor Model – SAM, https://sam.nrel.gov/, accessed 3 May 2025.
83 Z. Song, C. L. McElvany, A. B. Phillips, I. Celik, P. W. Krantz, S. C. Watthage, G. K. Liyanage, D. Apul and M. J. Heben, A technoeconomic analysis of perovskite solar module manufacturing with low-cost materials and techniques, *Energy Environ. Sci.*, 2017, **10**, 1297–1305.
84 T. Kobayashi, H. Katayama, Y. Kinden, Y. Kato, Y. Aya, T. Hashiguchi, D. Kanematsu, T. Kobayashi, A. Terakawa and H. Fujiwara, Cost-efficiency potential of solar energy on a global scale: Case studies for Si solar modules with PERC and heterojunction structures, *Prog. Photovoltaics Res. Appl.*, 2024, **32**, 799–813.
85 S. E. Sofia, H. Wang, A. Bruno, J. L. Cruz-Campa, T. Buonassisi and I. M. Peters, Roadmap for cost-effective, commercially-viable perovskite silicon tandems for the current and future PV market, *Sustain. Energy Fuels*, 2020, **4**, 852–862.
86 C. J. Mulligan, C. Bilen, X. Zhou, W. J. Belcher and P. C. Dastoor, Levelised cost of electricity for organic photovoltaics, *Sol. Energy Mater. Sol. Cells*, 2015, **133**, 26–31.
87 N. L. Chang, J. Zheng, Y. Wu, H. Shen, F. Qi, K. Catchpole, A. Ho-Baillie and R. J. Egan, A bottom-up cost analysis of silicon–perovskite tandem photovoltaics, *Prog. Photovoltaics Res. Appl.*, 2021, **29**, 401–413.
88 T. Kobayashi, H. Katayama, Y. Kinden, Y. Kato, Y. Aya, T. Hashiguchi, D. Kanematsu, T. Kobayashi, A. Terakawa and H. Fujiwara, Cost-efficiency potential of solar energy on a global scale: Case studies for Si solar modules with PERC and heterojunction structures, *Prog. Photovoltaics Res. Appl.*, 2024, **32**, 799–813.
89 S. E. Sofia, H. Wang, A. Bruno, J. L. Cruz-Campa, T. Buonassisi and I. M. Peters, Roadmap for cost-effective, commercially-viable perovskite silicon tandems for the current and future PV market, *Sustain. Energy Fuels*, 2020, **4**, 852–862.
90 P. Čulík, K. Brooks, C. Momblona, M. Adams, S. Kinge, F. Maréchal, P. J. Dyson and M. K. Nazeeruddin, Design and Cost Analysis of 100 MW Perovskite Solar Panel Manufacturing Process in Different Locations, *ACS Energy Lett.*, 2022, **7**, 3039–3044.
91 L. McGovern, E. Alarcón-Lladó, E. C. Garnett, B. Ehrler and B. van der Zwaan, Perovskite Solar Modules for the Residential Sector, *ACS Energy Lett.*, 2023, **8**, 4862–4866.
92 M. De Bastiani, V. Larini, R. Montecucco and G. Grancini, The levelized cost of electricity from perovskite photovoltaics, *Energy Environ. Sci.*, 2023, **16**, 421–429.
93 S. E. Sofia, H. Wang, A. Bruno, J. L. Cruz-Campa, T. Buonassisi and I. M. Peters, Roadmap for cost-effective, commercially-viable perovskite silicon tandems for the current and future PV market, *Sustain. Energy Fuels*, 2020, **4**, 852–862.
94 A. S. R. Bati, Y. L. Zhong, P. L. Burn, M. K. Nazeeruddin, P. E. Shaw and M. Batmunkh, Next-generation applications for integrated perovskite solar cells, *Commun. Mater.*, 2023, 1–24.
95 A. Martulli, N. Rajagopalan, F. Gota, T. Meyer, U. W. Paetzold, S. Claes, A. Salone, J. Verboven, R. Malina, B. Vermang and S. Lizin, Towards market commercialization: Lifecycle economic and environmental evaluation of scalable perovskite solar cells, *Prog. Photovoltaics Res. Appl.*, 2023, **31**, 180–194.
96 L. Wang, H. Zai, Y. Duan, G. Liu, X. Niu, Y. Ma, B. Li, Y. Sun, H. Zhou and Q. Chen, Cost Analysis of Perovskite/Cu(In,Ga)

Open Access Article. Published on 01 October 2025. Downloaded on 1/19/2026 7:04:07 PM.
This article is licensed under a Creative Commons Attribution 3.0 Unported Licence.

Se2Tandem Photovoltaic with Module Replacement, *ACS Energy Lett.*, 2022, **7**, 1920–1925.

97 K. A. W. Horowitz, R. Fu and M. Woodhouse, An analysis of glass–glass CIGS manufacturing costs, *Sol. Energy Mater. Sol. Cells*, 2016, **154**, 1–10.

98 *Cost Analysis of Tandem Modules*, IEEE Conference Publication, IEEE Xplore, https://ieeexplore.ieee.org/document/8366372, accessed 3 May 2025.

99 J. Wang, K. Li, J. Tang and C. Chen, A Perspective of Antimony Chalcogenide Photovoltaics toward Commercialization, *Sol. RRL*, 2023, **7**, 2300436.

100 R. Jones-Albertus, D. Feldman, R. Fu, K. Horowitz and M. Woodhouse, Technology advances needed for photovoltaics to achieve widespread grid price parity, *Prog. Photovoltaics Res. Appl.*, 2016, **24**, 1272–1283.

101 V. Fthenakis, E. Leccisi and P. Sinha, Life-Cycle Analysis of Potentially Longer Life Expectancy CdTe PV Modules, *IEEE Photovoltaic Specialists Conference*, DOI: 10.1109/PVSC48320.2023.10360051.

102 Z. Bao, Y. Luo, L. Wang, J. Dou, L. Wang, Y. Ma, Y. Du, Y. Lan, C. Zhu, H. Chen, H. Zhou, Y. Bai and Q. Chen, A Shortcut for Commercialization of Perovskites Solar Cells by a Recycling and Remanufacturing Strategy, *ACS Energy Lett.*, 2025, 1474–1482.

103 M. Cai, Y. Wu, H. Chen, X. Yang, Y. Qiang, L. Han, M. Cai, Y. Wu, L. Han, H. Chen, X. Yang and Y. Qiang, Cost-Performance Analysis of Perovskite Solar Modules, *Adv. Sci.*, 2017, **4**, 1600269.

104 L. A. Zafoschnig, S. Nold and J. C. Goldschmidt, The Race for Lowest Costs of Electricity Production: Techno-Economic Analysis of Silicon, Perovskite and Tandem Solar Cells, *IEEE J. Photovoltaics*, 2020, **10**, 1632–1641.

 © 2025 The Author(s). Published by the Royal Society of Chemistry